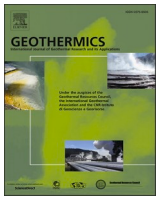
Geothermics 105 (2022) 102510



Contents lists available at ScienceDirect

Geothermics

journal homepage: www.elsevier.com/locate/geothermics





The dynamic evolution of the Lahendong geothermal system in North-Sulawesi, Indonesia

Lily Suherlina [a,b,c,*], Juliet Newson [a], Yustin Kamah [d,e], Maren Brehme [b,c]

[a] Iceland School of Energy, Reykjavik University, Menntavegur 1, 102, 101 Reykjavík, Iceland
[b] Geothermal Energy and Geofluids Group, Department of Earth Sciences, ETH Zurich, Sonneggstrasse 5, 8092, Zurich, Switzerland
[c] Helmholtz Centre Potsdam – GFZ German Research Centre for Geosciences, International Centre for Geothermal Research, Telegrafenberg,14473, Potsdam, Germany
[d] Upstream Technology Center Pertamina, Jl. Medan Merdeka, Timur no. 6, Jakarta, Indonesia
[e] PT. Geopatra Solusindo Energi Pratama, Jl. Tomang Raya 12F Jakarta Barat, 11430, Indonesia

ARTICLE INFO

Keywords:
Structural controls
Permeability changes
Fluid dynamics
High enthalpy system
Hydrochemistry
Well behaviour

ABSTRACT

This study uses an integrated approach to characterize the dynamic evolution of the power-producing high-enthalpy geothermal system of Lahendong, North-Sulawesi, Indonesia. Lahendong has two primary reservoirs, the southern and the northern, which have been utilised for electricity production for more than twenty years. The main focus of this study is the characterisation of heat and mass flows in the system with respect to geological structures and permeability distribution. Also, it delineates how the geothermal system has evolved and the spatial variation of the response resulting from prolonged utilization of the reservoirs. This research implemented geological structure analysis on recent surface fault mapping and pre-existing fault studies from literature. Further, the study analysed well data comprising well pressure, enthalpy, drilling program reviews and tracer tests. Hydrochemical investigation compiled new and old surface and subsurface hydrochemical evolution in both the temporal and spatial domain. The results confirm several fault trends in the study area: NE-SW and NW-SE are the major striking directions, while E-W and N-S are less dominant. The most apparent trends are NE-SW striking strike-slip faults, NW-SE thrust faults and N-S and E-W striking normal faults. The faults compartmentalize the reservoir. A comparison of the southern and the northern reservoir shows that the southern one is more controlled by faults; both reservoirs rely on fractures as permeability provider and are controlled by shallow hydrogeology, as derived from the integrated analysis of transient well data. Geochemical analysis shows that the reservoir fluids have generally a higher eelectrical conductivity and are closer to fluid-rock equilibrium, probably due to boiling, compared to spring waters. Spring waters have generally become more acidic, which is an expected result of reservoir boiling and increased steam input to near-surface waters. The spatial distribution of changes shows a permeability evolution over time and also the role of structural permeability in response to changing reservoir conditions. Observing and recording reservoir data is highly important to understand the reservoir response to production and ensure the long-term sustainability of the system. Additionally, the data is critical for making a major difference in the reservoir management strategy.

1. Introduction

During production, the initial equilibrium state in a reservoir and hydrothermal system develops into a transient state (Axelsson, 2008). The disequilibrium develops due to withdrawal of heat and mass via the wells being greater than the natural heat and mass input to the system. The fluid dynamics in the reservoir change rapidly, therefore careful monitoring is acquired to prevent or mitigate undesired changes in the geothermal system. These changes typically involve boiling in the upper zones of the reservoir due to pressure drawdown, increased flow of steam to the surface, or cold inflows to the hot reservoir (Addison et al., 2015). This study investigates permeability distribution, geological structures, and geochemical properties and their interaction to analyse the reservoir dynamics in the Lahendong field as a guide for reservoir management.

In this system, geological structures, i.e. faults, fractures or fault-related damage zones, play a vital role in fluid movement in the subsurface providing secondary permeability and by dividing the reservoir

* Corresponding author.
E-mail address: lsuherlina@ethz.ch (L. Suherlina).

https://doi.org/10.1016/j.geothermics.2022.102510
Received 12 February 2022; Received in revised form 11 June 2022; Accepted 25 June 2022
Available online 8 July 2022
0375-6505/© 2022 The Author(s). Published by Elsevier Ltd. This is an open access article under the CC BY license (http://creativecommons.org/licenses/by/4.0/).

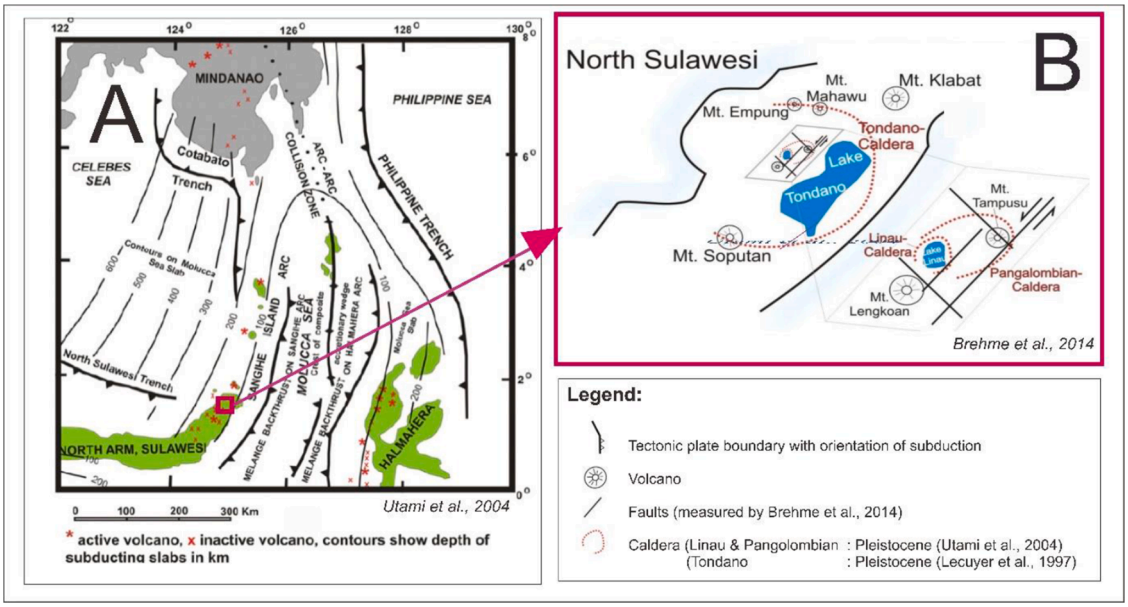


Fig. 1. Regional Geological Setting in North Sulawesi and the Lahendong field (modified from Utami et al., 2004 and Brehme et al., 2014).

into different compartments. They often control hydrothermal circulation, enabling infiltration of meteoric waters into the reservoir (Fauzi et al., 2015). Also, the drilling programs and well subsurface information provide important insights into location and orientation of structures. This is because wells primarily target fault structures with sufficient permeability (Axelsson et al., 2012). Additionally, tracer tests provide detailed information on fluid flow pathways in the reservoir (Axelsson et al., 2005). Hydrochemical properties of well and hot spring fluids are monitored to understand changes in the reservoir due to utilization. If the hydrochemical equilibrium is disturbed during production, element concentrations and physicochemical parameters change in well and hot spring fluids (Gao et al., 2019).

Some studies have investigated similar cases to evaluate reservoir dynamics as result of a continued utilization. Understanding geological structures and permeability, for example, are the crucial factor in understanding reservoir dynamics. In the case study in Rotokawa-New Zealand, Addison et al. (2015) observed a dominant structure play an important role in reservoir performance during utilization stage. This structure influences injection and production management which is vital to anticipate changes during reservoir conditions. The current study at the Lahendong field combines new and pre-existing structural knowledge to understand the role of faulting in the production and injection area. Information from drilling programs is also crucial to identify progression of well siting over time. The method, for example, has been used to observe permeability evolution and fault reactivation as result of reservoir dynamics in a critically stressed fault area (Siratovich et al., 2016; Anyim and Gan, 2020). Hydrochemistry analysis is another approach that has been widely used as an important tool for reservoir characterization (Wang and Zheng, 2019; Shi et al., 2017; Burnside et al., 2021) observing changes in fluids chemistry due to utilization is a powerful reservoir monitoring technique to understand the results of long-term utilization.

Investigation of reservoir dynamics has been an important instrument to understand geothermal system evolution as result of a continued utilization. An interesting study of the reservoir dynamics in the long-term production field has been given by Addison et al. (2015). He observed at Rotokawa field a strong decrease in pressure and temperature to support 172 MW operation. To increase a confidence of the underlying process towards the reservoir decline at the Rotokawa field, Addison et al., 2015 involved the cross-disciplinary approach (chemistry, geology, etc.). Another similar field with Lahendong is Tiwi as it has had intensive reservoir changes after 23 years production such as influx of meteoric waters and injected fluids, acidic fluids migration and a massive steam cap formation (Sugiaman et al., 2004).

All the above problems in a high-enthalpy geothermal field eventually will lead to a serious decrease in power production if not addressed. Prevention includes a combined observation of available datasets in the geothermal system to observe reservoir response during a long-term utilization. Preventative measures can be inferred from integrated studies (geoscience + reservoir data), and field investigations. These will be applied in the current study at the Lahendong geothermal field. The field produced 20 MW_e from power plant unit 1 since its inauguration in 2001 and increased the capacity up to 40 MW_e in 2007 by additional power plant unit 2. The power increased to 60 MW_e in 2009 generated by power plant unit 3, before it reached its maximum of 80 MW_e and power plant unit 4 in 2012. The initial reservoir system is liquid-dominated, observed at two reservoir blocks. The changes of pressure, enthalpy, and fluid chemistry occurred as a reservoir response to production, and these will be investigated using integrated instruments to ensure further field sustainability.

2. Geological setting at Lahendong site

Lahendong is located in Tomohon regency, North Sulawesi, Indonesia, approximately 30 km from Manado as the capital city. The Lahendong field is located on the northern arm of Sulawesi Island. Two active subduction zones (Fig. 1) form the Island; the first is Molucca trench in the eastern part, while the latter is Celebes trench in the northern part (Utami et al., 2007). Many calderas and faults are formed in the area of interest and its surrounding as result of the tectonic setting and extensive volcanic eruptions (Fig. 1). The four major fault trends are NE-SW, NW-SE, E-W and N-S oriented (Koestono, 2010). The geological and structural setting is also controlled by the volcano-tectonic depression of Tondano. Andesite, tuff, ignimbrite, sediment intercalations and volcanic breccia are the predominant rock types from the Pre-Tondano, Tondano, and Post-Tondano lithologies (Koestono, 2010; Sumintadireja et al., 2001). Several volcanoes (Mt. Soputan, Mt. Mahawu, Mt. Empung, Mt. Lengkoan, Mt. Tampusu) surround the Lahendong geothermal area. Linau hydrothermal crater appears in the center of the Lahendong field, now transformed into a crater rim with a lake (Lecuyer et al., 1997). Linau is an acidic-volcanic lake having pH 2-3, based on recent measurements (Brehme et al., 2019).

Table 1
Overview of fault observations from this study, if dip is not measured we assume the fault as vertical. Fault geometries have been checked mainly with the dataset given by Koestono et al., 2010 and Koestono, 2010.

Region	No.	Coordinate GPS (north)	Coordinate GPS (east)	Elevation (m)	Observation	Field Indicators	Remarks
West	1.	51 N 070 1894	140841	732	strike 100	ground alignments formed by dense grasses forming continuous lines	clear
	2.	51 N 070 1664	140973	707	strike 50	a small valley aligning with thermal manifestations, intersecting each other	clear
	3.	51 N 070 1833	140792	721	strike 130	a small valley aligning with thermal manifestations, intersecting each other	clear
	4.	51 N 070 1874	140810	737	strike 0	presence of shallow groundwater discharges accumulating along the lineament	clear
	5.	51 N 070 1978	141168	743	strike 80	clear exposed fractures surface with steep topography steps forming steep hills and ridges, with large surface manifestations around.	clear
	6.	51 N 070 2108	140938	753	dip angle 20, strike 165	andesite outcrops at an excavation where the layers clearly show andesite as the underlying layer with fresh unaltered texture	clear
North	7.	51 N 0704213	142674	820	strike 150	clear continuous alignments of abrupt topography steps	clear
	8.	51 N 0704406	142538	744	strike 170	clear continuous alignments of abrupt topography steps	clear
	9.	51 N 0703560	141808	807	strike 50	topography steps	hard to see
	10.	51 N 070 3750	141511	807	strike 170	continuous ground alignments which host a huge and active thermal spring at the intersection point	clear
East	11.	51 N 0704548	139307	789	strike 5	continuous topography steps with thermal manifestations along the area	clear
	12.	51 N 0704863	139626	914	strike 40	continuous topography steps with thermal manifestations along the area	clear
	13.	51 N 0704304	138935	930	strike 51	horst and graben features, with continuous topography steps and thermal manifestations	clear
	14.	51 N 0705997	141565	933	strike 80	topography steps with ridges and hills	clear
	15.	51 N 0705757	141059	933	dip angle 25, strike 350, dip direction 260	abundant hard, black, in-situ and fresh unaltered rock blocks (andesite) as a part of a major fault or big fracture planes	clear
	16.	51 N 0705765	141067	933	dip angle 50, strike 225, dip direction 315	abundant hard, black, in-situ and fresh unaltered rock blocks (andesite) as a part of a major fault or big fracture planes	clear
	17.	51 N 0705765	141067	933	dip angle 40, strike 200, dip direction 290	abundant hard, black, in-situ and fresh unaltered rock blocks (andesite) as a part of a major fault or big fracture planes	clear

3. Methods

3.1. Permeability distribution and geological structures

This section discusses approaches to understanding faults and fractures providing permeability and controlling fluid circulation in the Lahendong geothermal system. The methods used for this analysis include direct fault measurements in outcrops, well production characteristics, and tracer test analysis.

Three earlier fault studies are used as a solid foundation for the existing structural knowledge in the Lahendong field (Utami et al., 2004; Koestono et al., 2010; Brehme et al., 2014). Using various approaches and interpretations, the researchers have discovered new fault trends and confirmed several faults in the Lahendong field. Unfortunately, further structures controlling the Lahendong field, as well as their confirmations, are still strongly needed. Because the field is in a fracture-controlled environment, it is critical to conduct up-to-date structural observations.

The new fault measurement concentrates on the inferred faults and discovers new structures covering 7.82 km^2. The study collected data on fault locations including the strike and dip, as well as the sense of shear. We located structures in outcrops, hot springs and alignments and where possible measured displacement, and orientation. Geothermal surface manifestations often appear to be located along these structures and in this study are considered to be further evidence of faults.

Data on well targeting over time gives us information on the number and type of wells drilled per year (Table 1). Maps showing progression of the wells drilled over time are combined with fault maps, showing how an understanding of the system permeability has evolved over time (Figs. 3–5). Field production maps from three different years (2010, 2012, 2018) compare the change of production and reinjection zones over the years. Observations of individual well productivity after drilling gives information on subsurface permeability for each well. Combining all well information assists the identification of permeability distribution and explains changes in the reservoir production based on the permeability distribution.

The tracer test analysis focuses on interpreting fluid-pathways in the subsurface. In Lahendong, NDSA (Naphthalene di sulfonate acid) is injected in the reinjection well and flows towards production wells. The tracer profile exhibits breakthrough, the time of maximum concentration, the tracer pulse and mass recovery. The tracer analysis gives more insight into the hydrogeological conditions of the reservoir and the subsurface fluid pathways. Tracer data for this study are from Prabowo et al. (2015). There are 15 wells discussed in the paper, but this research only focuses on three production wells, providing the best data (LHD 5, LHD 8, LHD 11). This combines subsurface flow with the well drilling program and fault analysis.

Combining fault maps and drilling developments with production and tracer data provide information on structures and highly permeable zones at different time steps from exploration until recent utilization.

3.2. Hydrochemistry analysis

Fluid samples were taken from hot springs in the surrounding area according to the standards described in (Brehme et al., 2016). Seven deep production wells were sampled with a mini-separator for separating brine and steam at the wellhead keeping the fluid at pipe pressure without heat loss (Truesdell et al., 1987). The sampling locations can be seen in Fig. 10. Physicochemical parameters were measured in situ during the field visit including Temperature (T), Electrical Conductivity (EC), pH and bicarbonate concentration. The equipment used was from WTW (Wissenschaftlich Technische Werkstätten GmbH). The bicarbonate test is a titration field kit from Merck. Brine was collected and put into PTE bottles after filtration with <0.45 μm filters and acidification using HCl. Instruments used to measure the aqueous chemistry fluid concentration in the laboratory are: ICP AES, VISTA MPX, Varian and

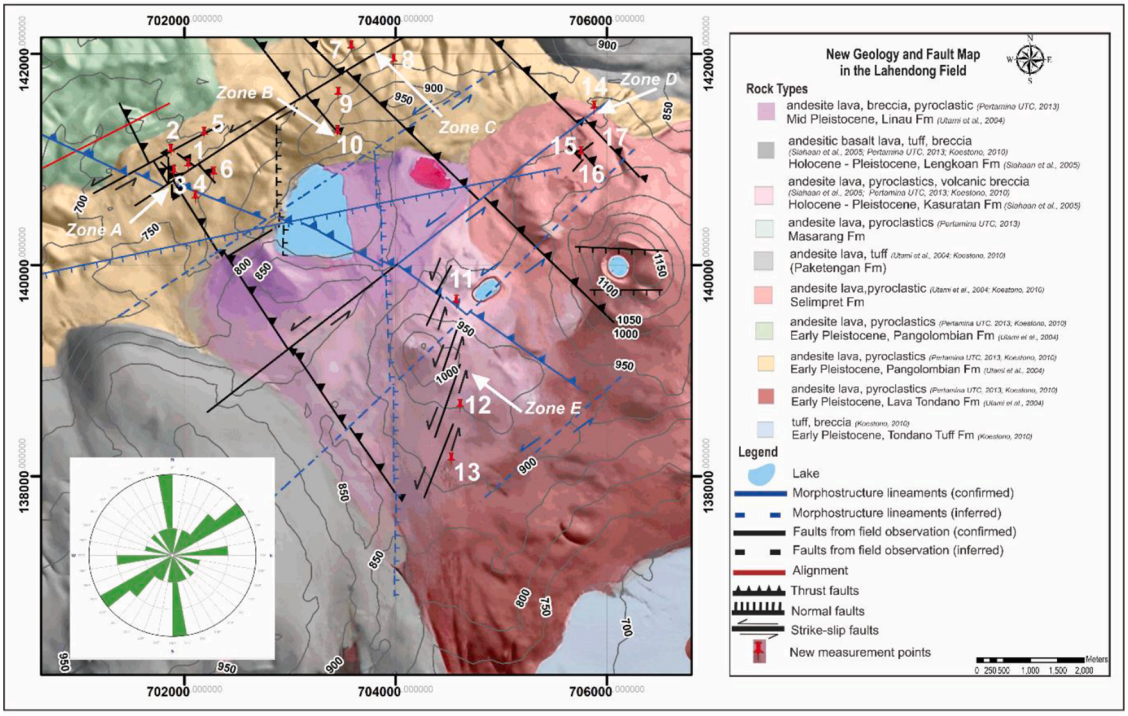


Fig. 2. Structural-geological map showing fault observations as indicated by red pins, where the number next to the box indicates the measurement points from the present study. Striking trends of the faults are given in the green rose diagram. The lithologies and the geological map are from PT Pertamina, 2015. (For interpretation of the references to color in this figure, the reader is referred to the web version ofthis article.)

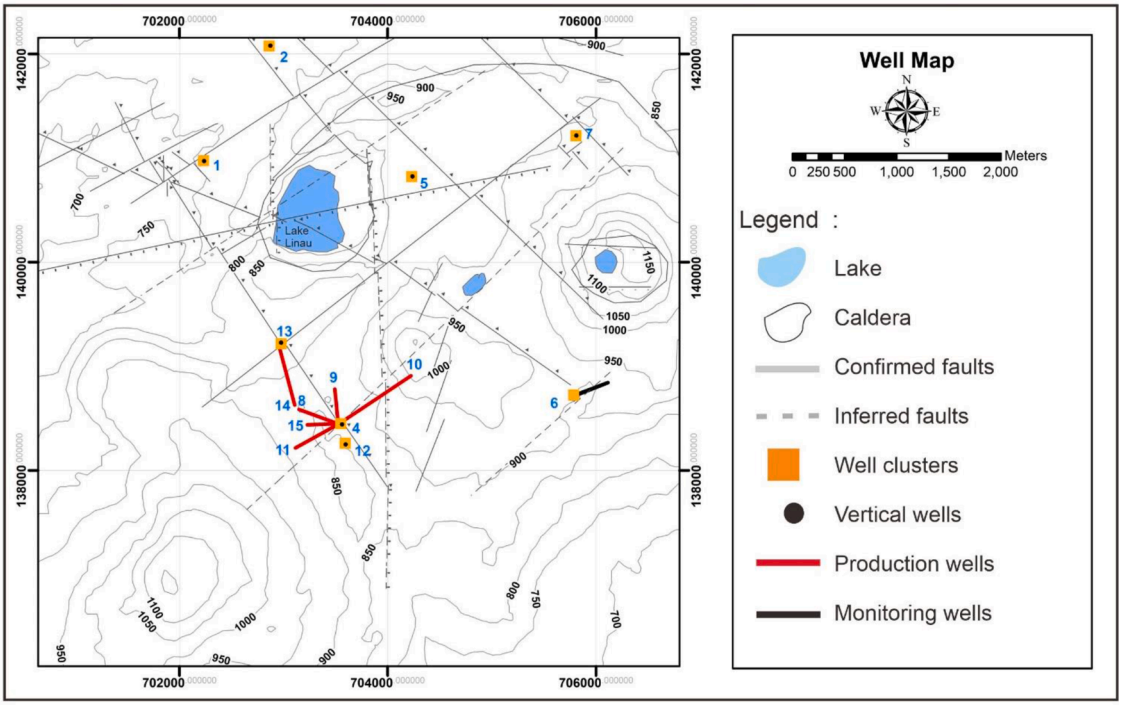


Fig. 3. Well map shows drilling locations and well directions until 2001 (modified from (Sumintadireja et al., 2001; Koestono, 2010) (map symbols as in Fig. 2).

Ion chromatography ICS 3000, Dionex. The hydrochemistry properties from the hot springs and wells are presented in Table 3.

The differentiation of water types (from wells and springs) throughout the study area is based on Electrical Conductivity (EC) and pH, and spatial analysis. It provides important information on the borders of reservoir partitions. In addition, temporal data is used to describe changes in the composition of water in surface springs and well fluids over time. In this study, we show fluid composition for October 2010, October 2011, March 2012, November 2012 and April 2018 using pH, electrical conductivity, and bicarbonate content.

Table 2
Detailed summary of wells progression history until 2001, 2012 and 2018

Year	Well	Location (north/ south)	Production /injection /monitoring	Productivity (MW_e) Approximation (Brehme et al., 2019)
	1	north	monitoring	
until 2001	2	north	monitoring	
	4	south	production	7
	5	north	production	5
	6	south	monitoring	
	7	north	injection	
	8	south	production	5
	9	south	production	
	10	south	production	5
	11	south	production	5
	12	south	production	5
	13	south	production	0
	14	south	production	0
	15	south	production	5
until 2010	16	south	monitoring	
	17	south	production	7
	18	south	production	7
	19	north	monitoring /production	0
	20	north	monitoring /production	0
	21	north	monitoring /production	0
	22	north	injection	
	23	north	production	20
	24	north	monitoring /production	0
	25	south	monitoring /injection	0
	28	north	production	20
	29	north	monitoring /production	0
	36	north	injection	
until 2018	37	north	production	3
	38	south	production	7
	39	south	monitoring /production	0
	45	north	monitoring	0
	47	south	monitoring /production	7
	48	south	production	7
	49	south	monitoring /production	0
	50	south	monitoring /production	-
	52	south	monitoring /production	-
	53	south	monitoring /production	-
	54	north	monitoring /production	-

4. Results

4.1. Review of faults controlling the Lahendong system

Utami et al. (2004) identified the Pangolombian caldera, Linau crater, NE-SW trending and NW-SE trending faults as major geological structures in Lahendong. The structures were defined from aerial photographs, ground mapping and borehole studies. Alignment of the active thermal manifestations confirmed several fault locations, in particular NE-SW and NW-SE trending faults. Nevertheless, her study has not unveiled the type of faults. A later study (Koestono, 2010) defined the occurence of: (i) normal to strike-slip NE-trending faults, (ii) strike-slip E-trending faults; and (iii) NW- to N-trending normal faults. Some of these faults are inferred and some described to possibly have an increased permeability. Brehme et al. (2014), describe normal to oblique-slip left-lateral movement on NE-SW striking faults according to Riedel shears and slickensides dipping 72° and 81° towards SE. Faults striking E-W and N-S are considered as normal faults based on evidences from topography and outcrops.

Based on these previous studies, additional structural-geological investigations have been carried out to confirm the remaining inferred faults (Fig. 2). The investigations comprised six observations in the west, four points in the north, four points in the east and three points in the south. An overview of the observations is given in Table 1.

We discovered six apparent faults in the western region of interest (No. 1-6 in Table 1). They are found on the west shore of Lake Linau, namely in the Lahendong cemetery region (Zone A, Fig. 2). Ground alignment, thermal manifestations, and topography within the area all prove the existence of these faults. The initial observation (No 1) is clear ground alignments formed by fractures where dense grasses display continuous lines, striking 100° (NW-SE). Locality No. 2 and No. 3 are in a small valley aligning with thermal manifestations, that also intersect. The structures strike in 50° NE and 130° NW-SE, respectively, according to the measurements. The fourth observation location (No. 4) strikes N 0°, where shallow groundwater discharges and accumulates along a lineament. Exposed fracture surfaces at No. 5 strike 80° ENE with steep topography steps and form steep hills and ridges, which could also be an indication of faults. The existence of faults is supported at the sixth observation (No. 6) where andesite outcrops with fractures striking 165° NW-SE and dipping 20°.

Four locations were visited in the northern region. The main focus of investigation is within the inferred faults area of Pangolombian rim (Zone B, Fig. 2) and the northeastern Lake Linau (Zone C, Fig. 2). The Pangolombian rim is mostly covered by dense-vegetation and forests. Therefore, the most obvious fault indication is by clear continuous alignments of abrupt topography steps. Two measurement points recorded two faults striking 150 ° – 170 ° toward NW-SE (No. 7 and 8). In the same area, additional measurements were made in the northern Linau crater. Some noticeable indications of faults include clear topography steps and thermal springs. The measurements exhibit two faults striking 50 ° NE and 170 ° NW-SE (No. 9 and 10). The former is harder to see in the topography, while the latter shows clear continuous alignments and hosts huge thermal springs at an intersection point.

The observation in the eastern region took place in two different survey areas. The first is near to the reinjection wells of Lahendong (Zone D, Fig. 2) and the second is in Kasuratan area (Zone E, Fig. 2). In the area of reinjection clusters (No. 14-17), there are four identified faults striking in different directions. Topography steps showing ridges and hills in measurement No. 14 delineates a fault striking 80 NE. In addition, abundant hard, black, in-situ, and fresh unaltered rock blocks, believed to be andesites, occur in the location. The rocks represent a piece of major fault or larger fracture planes. Three rock planes (No. 15,16,17) reveal three fractures each striking 260°, 315 °, 290 °.

The measurement Zone E is difficult to access due to abundant vegetation. Therefore, the observation points took place from an adjacent hill. Thermal manifestations were also discovered along the survey area. Two clear fault structures appear to strike at 5 ° and 40 ° NE along the area with continuing topography steps (location No. 11 and 12). The additional features showing horst and graben are present in the area (No. 13) showing structures striking 51° NE. The structures have a clear trend and could be seen from far away.

Photographs of field evidence that are strong indicators of the presence of faults are given in Appendix A, Appendix B and Appendix C. The first and second appendices show the intersection of two faults, where manifestations emerge at the intersection point. The last appendix shows an outcrop, where fault 6 is clearly visible. Those evidences can also be used to support fault indicators for other regions in the same stress setting, such as points 15–17. Around the points, faults indicators are less sufficient due to hard accessibility of the places. As a result, the fault indicators in points 1-6 can be extrapolated to confirm faults in points 15-17. Moreover, faults 15 and 16 have the same fault setting as faults 2 and 3 where intersection points occur.

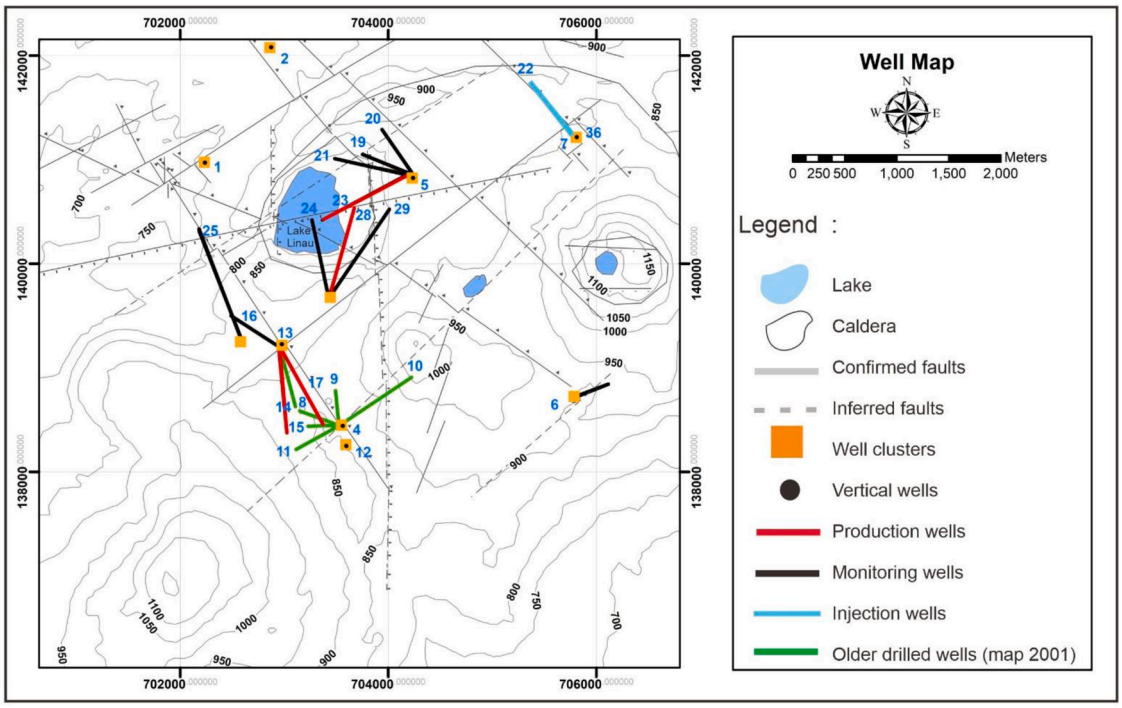


Fig. 4. Well map showing drilling locations and well directions until 2012 with 80 MW_e installed capacity (modified after Brehme, 2015) (map symbols as in Fig. 2).

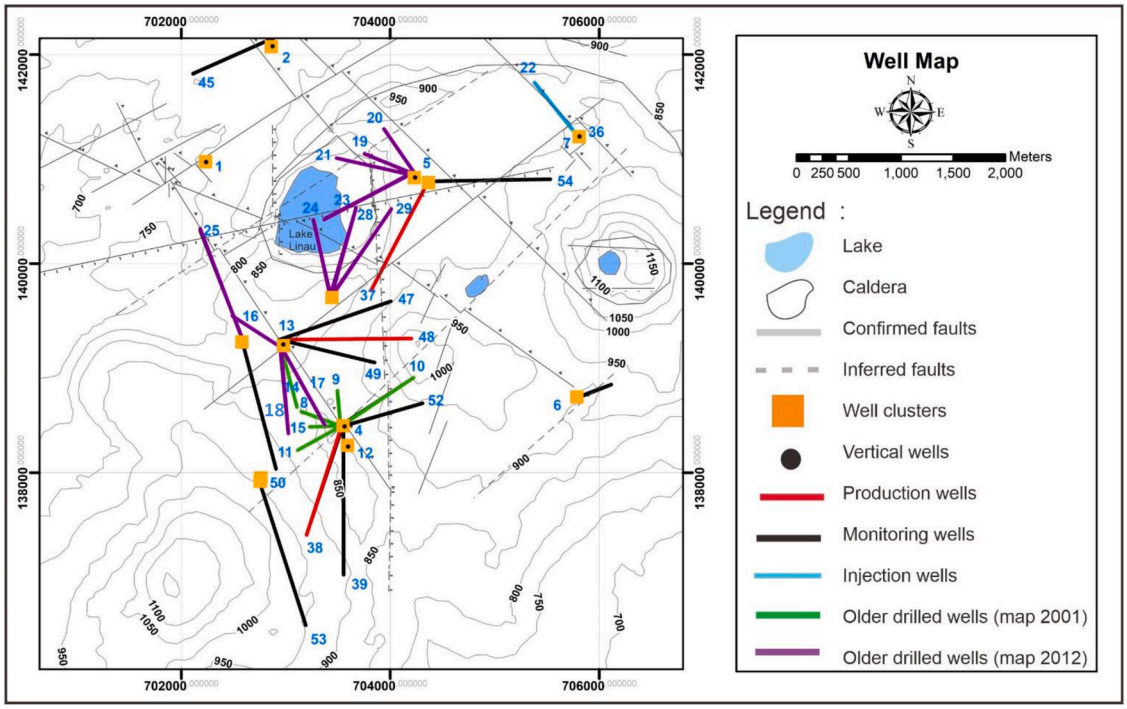


Fig. 5. Thirty-eight wells are drilled in Lahendong field in the two systems until April 2018 (map symbols as in Fig. 2)

The integration all previous and current fault observations allow us to categorize the following groups of faults for the Lahendong geothermal field, sorted by appearance: (1) NE-SW (from N5^o to N80^o) trending strike-slip faults, (2) NW-SE (from N130^o ^{to} N170^o) trending thrust faults dipping 20^o, (3) N-S and E-W trending normal faults dipping N78^o and E88^o. The new fault observations justify these striking trends as indicated by the rose diagram (Fig. 2). Strike-slip faults striking NE-SW appear in the north and south and together with NW-SE striking thrust-faults they play the most important role for the Lahendong reservoir. Less essential faults are striking N-S and E-W.

Four sinistral strike-slip faults are evident in the Lahendong area, with Sigma1 striking NNW-SSE, which results in extensional strain in a left step-over area and compressive strain at a right step-over due to fault-block movement. Normal faults separate extensional basins and are dominated by dilational zones, while the thrust faults link the right step-over sinistral faults. A second relatively younger faulting phase

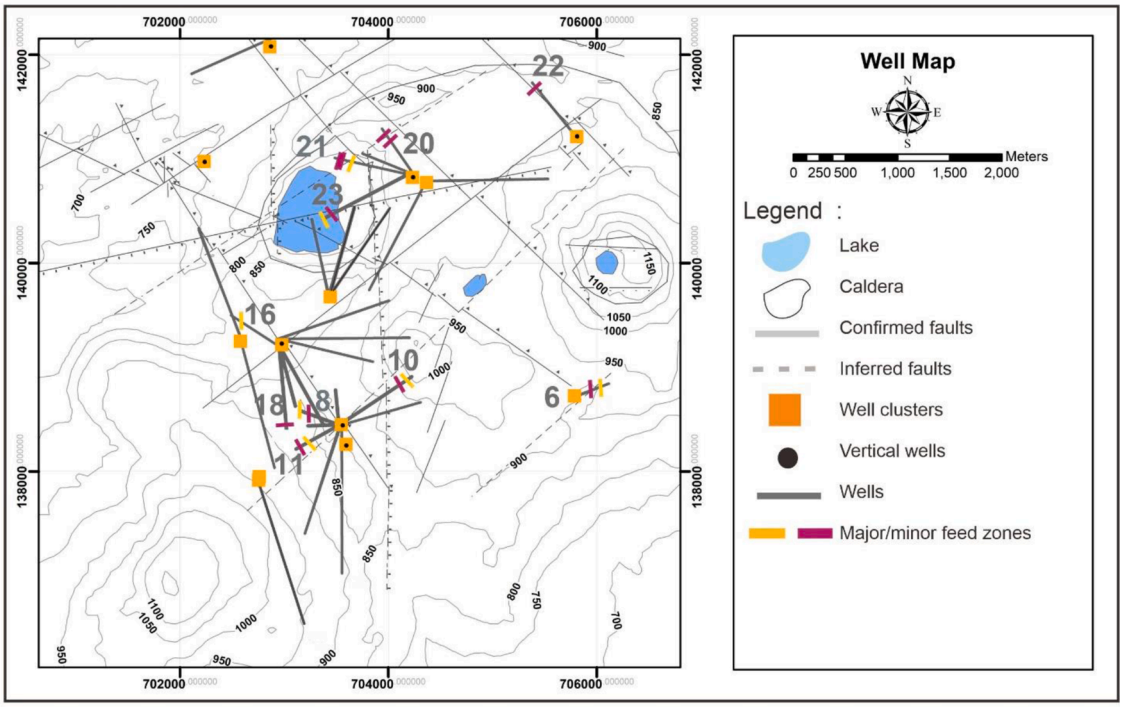


Fig. 6. 2D view of locations of major feed zones (yellow box) and minor feed zones (purple box) in selected wells (map symbols as in Fig. 2). (For interpretation of the references to color in this figure, the reader is referred to the web version ofthis article.)

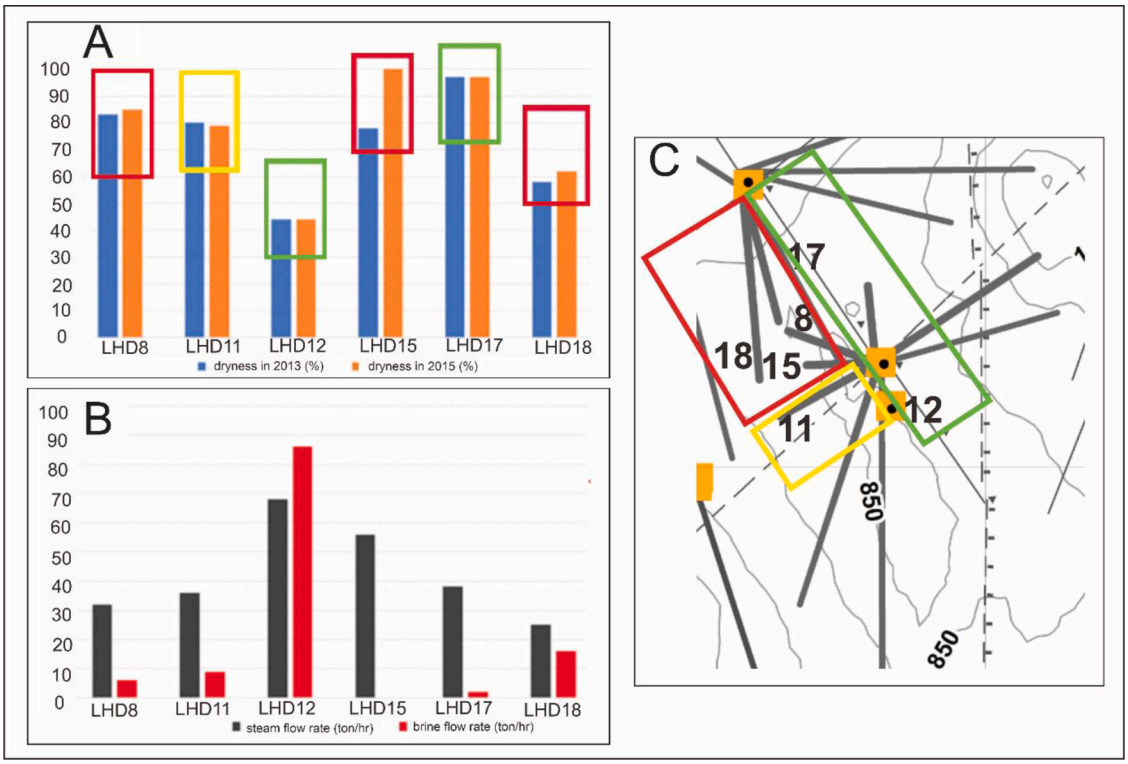


Fig. 7. (A) Comparison of the dryness in production wells in the southern area in 2013 (source: (Permana et al., 2015) and 2015 (source: PT. Pertamina), (B) mass flow rate in ton/h for steam and brine in southern wells in 2015 (source: PT. Pertamina), (C) locations of wells in map (the map symbols as in Fig. 2). The red, green and yellow boxes represent dryness trends in the wells respectively for increasing, stable and decreasing dryness. (For interpretation of the references to color in this figure, the reader is referred to the web version ofthis article.)

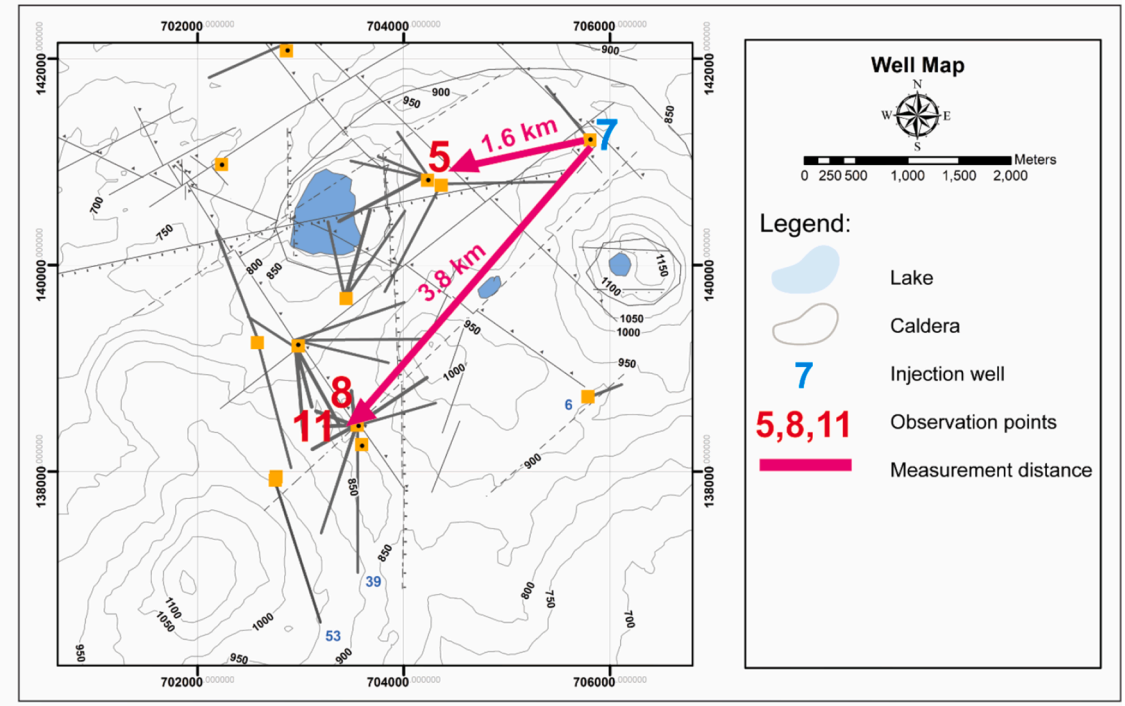


Fig. 8. Set-up of the tracer test measurement, where the pink line shows the distance from injection point to observation wells (the map symbols as in Fig. 2). (For interpretation of the references to color in this figure, the reader is referred to the web version ofthis article.)

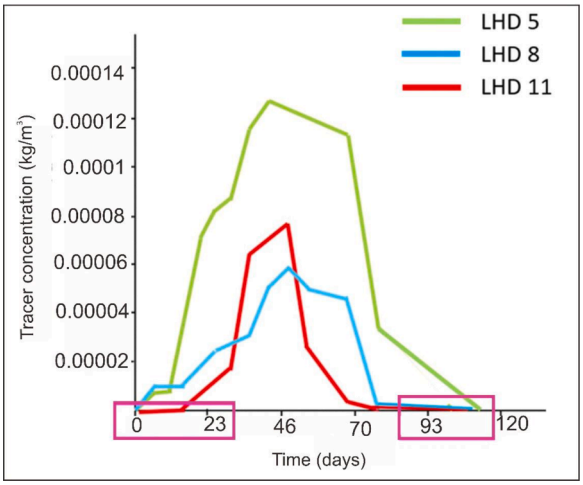


Fig. 9. Tracer response curves for three wells (modified from (Prabowo et al., 2015)), the pink rectangle shows undetectable tracer signals on certain days at the well. (For interpretation of the references to color in this figure, the reader is referred to the web version ofthis article.)

resulted in perpendicular normal faults. This faulting phase is believed to be characterized by regional cooling processes (Brehme et al., 2014).

4.2. Drilling program in Lahendong

Understanding drilling programs at different timesteps can increase the knowledge of well siting, well trajectories, well classification, and which structures they appear to intersect. The current study reconstructs the previous 2D maps of the 2010 and 2015 drilling programs with the new fault model. The reconstruction revises structural and permeability knowledge with respect to well siting and site selection. Another new contribution from the recent study is reconstruction of the new drilling map (2018) which shows the newest well progression. The reconstruction of the drilling maps with the updated faults increases the understanding of structures of interest and permeability targets over time.

The initial exploration of the Lahendong system began in the 1970s with drilling of seven wells (Fig. 3): LHD 1 and LHD 5 in the northern block, LHD 4 in southern block and LHD 13, LHD 6 and LHD 7 off the central region of Lahendong (Siahaan et al., 2005). Prior to 2001, fifteen wells were drilled, comprising seven exploration and eight production wells. One exploration well (LHD 7) in the north-east became the first reinjection well in the Lahendong geothermal system. The generation of the first 20 MW_e from Unit 1 since 2001 was achieved by using LHD 4 – LHD 15 from the southern reservoir (Fig. 3) (Sumintadireja et al., 2001; Koestono, 2010).

The initial development of production wells up to 2001 indicated a good reservoir in the southern area. Most of the boreholes drilled in that area are close to major known faults, which are believed to have a good permeability (Sumintadireja et al., 2001). This assumption is confirmed by large lost circulation zones in those wells (Yani, 2006). More wells are drilled over time to meet the production demand and details of the wells progression history that can be seen in Table 2. The locations and trajectories of wells drilled up to 2012 and 2018, respectively, are presented in Figs. 4 and 5. In the Lahendong field, power plant Unit II has generated additional power of 20 MW_e since 2007, followed by Unit III producing additional 20 MW_e, in operation since 2009 and Unit IV with 20 MW_e since 2012.

Structural permeability in the south is seen in the feed zone distribution related to faults (Fig. 6). Feed zones are more predominant in the south than in the north. Assuming a dip towards NE of the thrust fault located to the south-west of LHD 16, LHD 8, LHD 15, LHD 18 and LHD 11, as well as a vertical NE trending fault near LHD 10 and LHD 6, most wells intersect faults at the depth of the feed zones. In the south, the feed zones appear to be related to NE-SW and NW-SE structures, while in the north feed zones most probably intersect the inferred NE-striking fault near cluster 5.

Changes in individual well behaviour during production also provides information on the Lahendong reservoir. These changes are

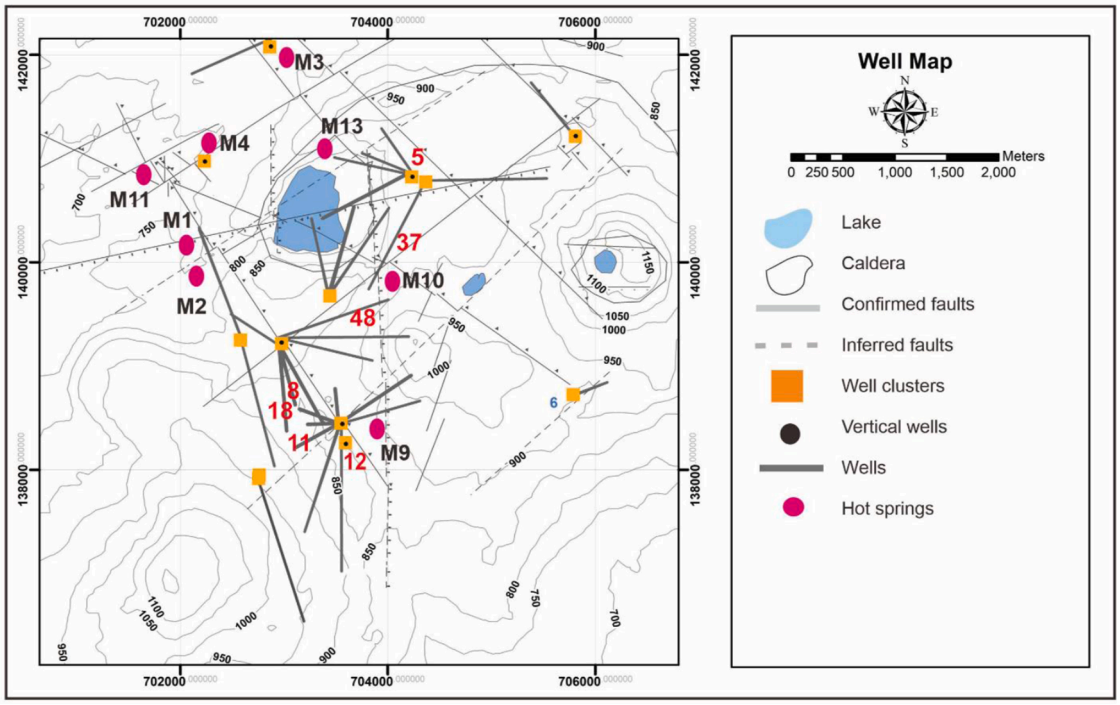


Fig. 10. Location of sampled hot springs and wells in the Lahendong geothermal area (the map symbols as in Fig. 2).

primarily thermodynamic changes and/or changes in flow rate. Evidence for a decline in well productivity and possibly reservoir pressure can be seen in the number of make-up wells drilled in the southern region in order to maintain production. The southern reservoir response to production can also be seen in the change of dryness of the produced fluid (Fig. 7 A) in 2013 and 2015.

In general, there are three trends in Fig. 7 A: an increasing dryness (represented by red box, LHD 8,15,18), a stable dryness (represented by green box, LHD 12,17) and a decreasing dryness (represented by yellow box, LHD 11). Overall, the total dryness is high, starting from 45% up to nearly 100% in 2013 and 2015 (Fig. 7 A). The increasing dryness in production wells is a result of pressure drawdown leading to boiling due to fluid extraction. The high dryness (> 45%) of some wells also indicates that the southern reservoir contains zones of two-phase fluids. Ghilmana et al. (2015) supports this interpretation; showing well LHD 17 in the south producing vapour although another well in the same well pad produces lower enthalpy fluids (more brine). LHD 17 turned into a dry-steam well in April 2018 (source: personal communication with site owner).

4.3. Tracer data analysis

Tracer test data and analysis for this study refers to Prabowo et al. (2015). There are 15 wells discussed in the paper, but this study only focuses on three wells of interest: LHD 5, LHD 8, LHD 11. The tracer test results give information on subsurface flow from the interpretation of mass recovery and time breakthrough data. We aim to understand reasons for changes in dryness in some wells.

NDSA (Naphthalene disulfonate acid) has been injected into LHD 7 at 40° C. The mass of injected tracer in LHD 7 is 100 kg. The test scenario is presented in Fig. 8. It shows reinjection well LHD 7 as the starting point of tracer flow towards northern (LHD 5) and southern production wells (LHD 8, LHD 11). The distance is 1.6 km and 3.8 km respectively (drawn as a bold pink line). Fig. 9 shows the tracer return profile in the three wells with mass concentration over time. The profile shows a relation between tracer breakthrough and maximum fluid velocity. The time of maximum concentration is the average fluid velocity, the tracer pulse width associates with dispersion along flow-paths while the mass/tracer recovery is a function of time (Axelsson et al., 2005). Interpretation of the tracer profile in this study only focuses on qualitative analysis.

The first thing to observe in Fig. 9 is the width of the dispersion profile. The broader the dispersion profile, the more 'spread out' the tracer is in the subsurface through indirect fluid pathways. In general, Fig. 9 shows that LHD 5 and LHD 8 have a broader profile indicating an indirect connection between injector and producer well. A sharper tracer return in LHD 11 reflects a more direct connection with less dispersion from injector LHD 7 to the producer LHD 11.

Tracer breakthrough is the time at which a tracer first arrives in the production well. In general, tracer tests can last a few weeks, months or even years which are very dependent on distances and real fluid pathways (Axelsson et al., 2005). The longer the distance, the later the tracer will be received in the production well. Fig. 9 generally shows fast breakthroughs in LHD 8 and LHD 5 within less than ten days, while the red line (LHD 11) is the slowest (more than 10 days).

4.4. Hydrochemistry of hot springs and wells

Seven spring waters (Fig. 10) sampled in 2018 were found to be strongly acidic (pH: 1.51-2.89); the electrical conductivity (EC) is 487-6320 μS/cm; the redox potential ranges from 87.1 up to 557.1 mV, and temperature (T) ranges from 24.9 - 67 °C (Table 3). Major components in the spring water are Si, Fe, Al and Ca with total concentrations of 555 mg/l, 463.5 mg/l, 268 mg/l and 156 mg/l, respectively. The most dominant anion is SO_4 with the highest concentration of 7588.7 mg/l.

Additionally, seven wells were sampled (Fig. 10.): LHD 5, LHD 8, LHD 11, LHD 12, LHD 18, LHD 37, and LHD 48. The well waters show a pH range of 4.79-8.7, HCO_3^- between 16.03 -115.38 mg/l, the electrical conductivity (EC) ranges from 1079-2550 μS/cm, the redox-potential is around -213.6 to -1799 mV. Major ions in the water are Cl, Na and Si with total concentrations of 2621.54 mg/l, 2148 mg/l and 1878 mg/l, respectively (Table 3).

According to Fig. 11 A (Giggenbach diagram), the hot spring waters from Lahendong can be described as sulphate waters. The high SO_4 content in volcanic systems is mainly generated by oxidation of H_2S to

Table 3
New hydrochemical database of hot spring waters and well waters, where (-) means no measurement

Hot Springs	pH	T sampling	EC	Redox	Al	Ba	Ca	Fe	K	Mg	Mn	Na	Si	Sr	Zn	F	Cl	SO_4	NO_3	PO_4
units		(°C)	µS/cm	mV	mg/l	mg/l	mg/l	mg/l	mg/l	mg/l	mg/l	mg/l	mg/l	mg/l	mg/l	mg/l	mg/l	mg/l	mg/l	mg/l
M2	1.82	54.8	2980	302.7	21	0.05	6.3	8.2	2.9	2.7	0.13	4	57	<0.05	<0.05	<0.25	8.58	874.52	<0.75	<1
M4	2.37	43.6	1560	87.1	27	0.05	6.6	7	1.5	3.9	0.18	2.7	42	<0.05	<0.05	2.21	5.01	504.95	<0.75	<1
M9	2.22	45.1	2340	557.1	44	0.05	17	23	3.4	8.6	0.50	9.1	72	0.08	<0.05	2.24	8.66	813.59	<0.75	<1
M10	2.67	24.9	3880	133.7	94	0.05	105	382	18	51	6.8	64	161	0.31	0.25	4.5	19.66	2796.8	<0.75	15.41
M13	1.51	60	6320	281.2	72	0.05	1.5	26	0.90	1.8	0.08	0.78	137	<0.05	0.05	<0.25	19.89	2205.51	<0.75	<1
M3	2.80	30.7	838	245.6	3.6	0.05	7.6	12	17	3.2	0.13	5.4	45	<0.05	0.05	0.9	13.15	178.31	<0.75	<1
M11	2.89	67	487	528	6.8	0.05	12	5.3	3.2	4.3	0.29	5.2	41	0.07	0.07	0.51	2.49	215.05	<0.75	<1
Wells	**pH**	**T reservoir**	**EC**	**Redox**	**HCO_3-**	**Al**	**Ba**	**Ca**	**Fe**	**K**	**Mg**	**Mn**	**Na**	**Si**	**Sr**	**Zn**	**F**	**Cl**	**SO_4**	**NO_3**	**PO_4**
units		(°C)	µS/cm	mV	mg/l	mg/l	mg/l	mg/l	mg/l	mg/l	mg/l	mg/l	mg/l	mg/l	mg/l	mg/l	mg/l	mg/l	mg/l	mg/l	mg/l
LHD 5	8.7	232	1847	-213.6	115.38	1.1	<0.05	5	<0.1	37	<0.1	<0.05	349	234	0.05	<0.05	4.14	318.44	165.04	<0.75	<1
LHD 8	6.87	316	2130	-296	67.31	0.43	<0.05	5.8	<0.1	38	<0.1	<0.05	389	186	<0.05	<0.05	3.98	449.08	102.87	<0.75	<1
LHD 11	7.77	312	1154	-394.5	80.13	0.32	<0.05	7.2	<0.1	26	<0.1	<0.05	208	213	<0.05	<0.05	3.41	193.04	118.28	<0.75	<1
LHD 12	4.79	327	1380	-241.5	16.03	0.39	<0.05	1.9	0.34	65	<0.1	<0.05	213	270	<0.05	<0.05	2.99	354.58	41.04	<0.75	<1
LHD 18	7.36	287	2550	-257.4	35.26	0.60	<0.05	2.8	<0.1	94	<0.1	<0.05	433	337	<0.05	<0.05	4.95	669	69.75	<0.75	<1
LHD 37	8.44	-	1962	-235.7	96.15	1	<0.05	11	<0.1	36	<0.1	0.07	374	275	0.10	<0.05	3.63	398.43	123.38	<0.75	<1
LHD 48	6.15	-	1079	-1799	35.26	1.1	<0.05	3.8	<0.1	41	<0.1	<0.05	182	363	<0.05	<0.05	4.24	238.97	55.43	<0.75	<1

SO_4 and by rock dissolution (Ármannsson, 2009). Spring waters plotting within the Mg corner (Fig. 11 B) have an immature fluid composition, which is not in equilibrium with rocks and the composition being most likely a result of absorption of dissolved rock (Reyes and Hutt, 2000). According to these two diagrams (Na-K-Mg and Cl-SO_4-HCO_3), surface spring water compositions are dominated by rock dissolutions and do not directly originate from deep thermal waters. Therefore, they cannot be used to directly extrapolate to subsurface properties.

Characterization of well waters is done using the Giggenbach ternary diagram Cl-SO_4-HCO_3 (Fig. 11 A). It shows that all wells plot in the Cl corner (chloride fluid type) with minor sulphate concentrations. The Na-K-Mg diagram shows that the geothermal well waters are in equilibrium with the rocks, plotting in the full equilibration area.

4.5. Spatial analysis of hot springs and wells

Analysis of spatial distribution of hot spring waters based on Electrical Conductivity (EC) indicates two main groups: waters with higher EC shown in bold lines and lower EC waters shown in dashed lines (Fig. 12). The blue areas represent data recorded in 2012, whereas the red region is from measurements in 2018. In this study, the higher EC refers to the spring and well fluids with an EC of >1500 µS/cm, while the lower EC refers to fluids with less than 1500 µS/cm.

In 2018, the high electrical conductivity of hot spring waters was observed in the central study area and southwest of it (Fig. 12). A possible reason for this distribution is a higher density of fractures in the south and therewith more fluid flow pathways towards the surface. Large areas of leached rocks are the result of these intense fluid-rock interactions. The higher permeability also enables gases e.g., H_2S, from the reservoir to rise to the surface and condense in groundwater, forming low pH fluids which leach the cations out of the rock, forming hydrothermal clays (Nicholson, 1993). The northern area shows lower electrical conductivity and especially lower sulphate concentrations. In that region less fluid-rock interaction leads to less alteration and mineral leaching. Compared to 2018, in 2012 (Fig. 12) the higher electrical conductivity waters were observed more towards the northwest.

Spatial distribution of well waters in 2018 revealed higher EC values expanding from the north to the south-western region, whereas the lower EC spreads more in the south-eastern area (Fig. 13). Higher electrical conductivity in deep fluids originates from leaching processes in the reservoir rocks, the mixing with deep magmatic fluids or from concentration of salts due to boiling (Arnórsson et al., 2007). The two different electrical conductivity groups occur close to each other and might be separated by a fluid barrier (impermeable fault) preventing the waters from mixing.

4.6. Temporal changes on hot spring and wells

To investigate temporal changes of spring waters in Lahendong, we compared hydrogeochemical data from October 2010, October 2011, March 2012, November 2012 and April 2018. The data from each spring is plotted over time to show chemical changes of the waters. Fig. 14 shows the changes in electrical cconductivity (EC) and acidity (pH).

Overall, we observe a correlation between EC and pH trends. The upward trend of EC in hot springs relates to a downward trend in pH and vice versa. For instance, M4, which has a low pH of <2 (March 2012 - November 2012) and a very high EC, while it shows a decreasing EC in 2018 and an increasing pH. This is most likely related to extensive leaching as a result of aggressive pH. The dissolved minerals cause an increase in dissolved elements and increasing conductivity.

5. Discussion

5.1. Permeability distribution and geological structures

Recent observations of additional faults in Lahendong clearly

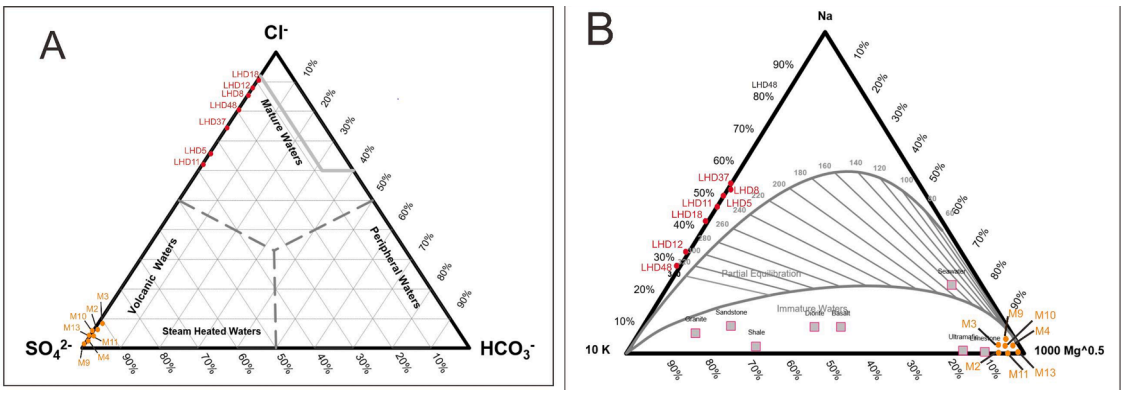


Fig. 11. Ternary diagrams show spring (orange colour) and well water (red colour) characteristics in 2018. (For interpretation of the references to color in this figure, the reader is referred to the web version ofthis article.)

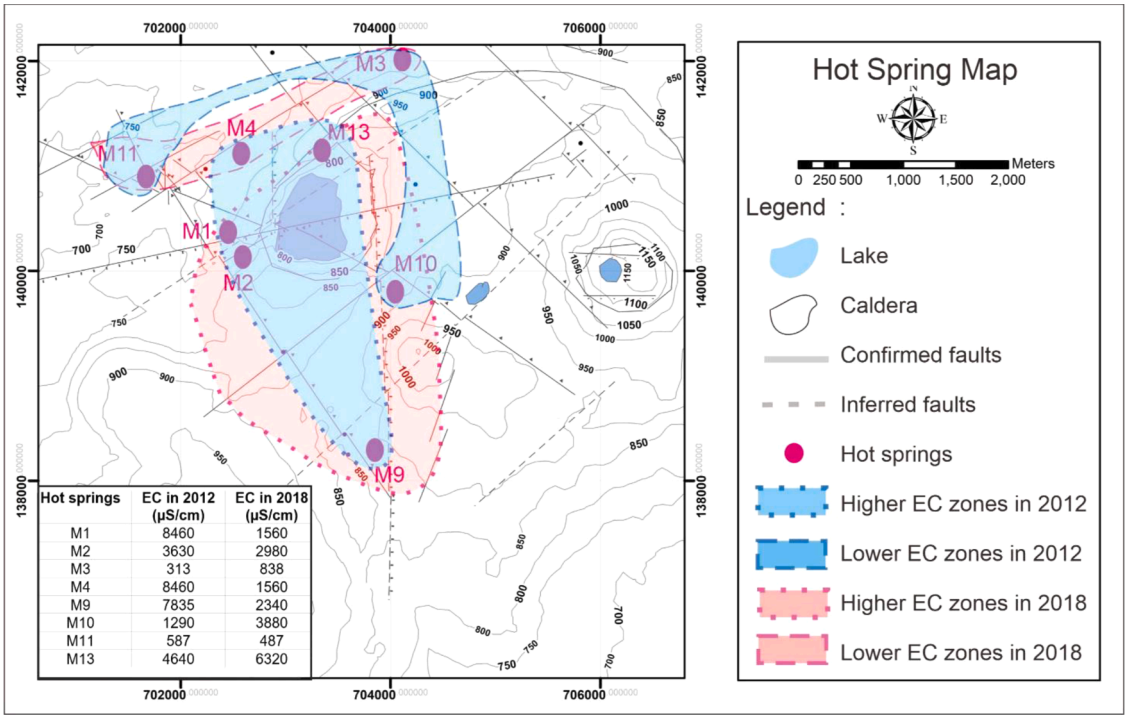


Fig. 12. Spatial distribution map of hot springs based on Electrical Conductivity (EC) value in 2012 and in 2018 (the map symbols as in Fig. 2).

revealed that the most dominating fault patterns are NE-SW and NW-SE oriented with N-S and E-W trending faults being less dominant. The most obvious NE-SW and NW-SE fault patterns are observed in the south of the study region. The NW-SE striking faults play a key role for linking fluid recharge of some the southern producing wells, in particular LHD 8, LHD 11, whereas the NE-SW striking fault close to well 12 (fault A, Fig. 16) most probably acts as a boundary, indicated by the fluid patterns of well dryness (Fig. 7) and pH, EC, and mass flow rate on Fig. 16. In the northern area, the role of N-S and E-W striking faults, particularly around Lake Linau, needs additional investigations.

In the Lahendong field, different well progression over time provides crucial information on reservoir behaviour and structural configuration. To exemplify, Table 2 highlighted that LHD 13 and LHD 14 experience a high dryness despite targeting a fault zone. The boreholes produce 0 MW_e (Brehme et al., 2019) indicating they are non-productive. Although the wells are located in the fault zone, there might be a number of reasons why they are not producing. The most likely reason can be due to a poor local fracture connection near the boreholes, which prevents fluid exchange with the drill-hole. Drilling a well near the fault regime is not always a guarantee to generate productive wells because other factors might be at play (Axelsson, 2013). The borehole closest to LHD 13 and LHD 14 is LHD 18. This well was drilled in the same well pad as LHD 13 and LHD 14 and is capable of producing moderate power of 7 MWe (Brehme et al., 2019). It reflects a good fracture-connectivity.

Two productive wells (LHD 23, LHD 28) in the northern reservoir yield 20 MWe each and are situated between the estimated N-S and E-W faults in a good structural environment. Despite the fact that the wells are still producing, they have a declining productivity. Furthermore, the wells have a strong hydraulic connection to Lake Linau, which is located above the wells. The lake water and well water is strongly acidic, with a pH below 3 (based on our last lake measurements in 2018). LHD 23, LHD 28 hit an acidic reservoir in the north above 1500 m depth, according to cross sections by (Brehme et al., 2014). The pH of the wells are 2.7 and 3.2 for LHD 23 and LHD 28 measured during a previous field campaign (Brehme et al., 2014).

The well development at certain times, moreover, reported dryness behaviour in reservoirs. In this study, the dryness rate equals the fraction of steam in wt% in the production boreholes (Pratama and Saptadji,

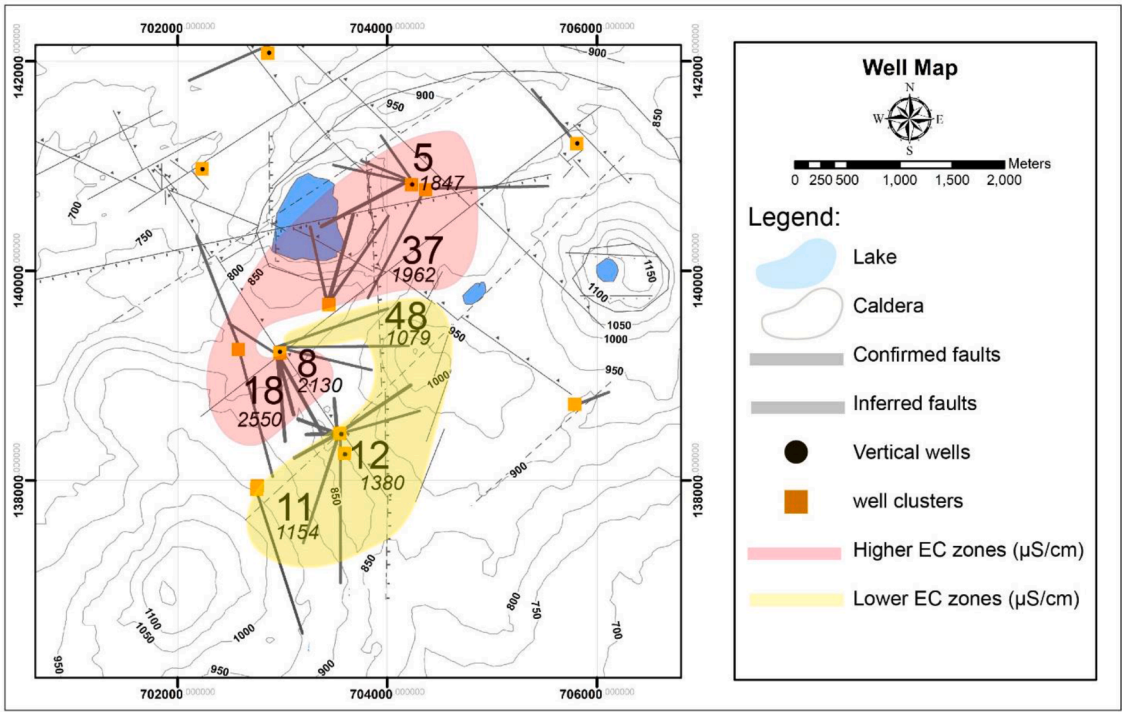


Fig. 13. Spatial distribution map based on Electrical Conductivity (EC) for well waters in 2018 shown in bold letters (the map symbols as in Fig. 2).

2016). The three different trends of increasing, stable or decreasing dryness in wells close to each other indicate boundaries between the differently behaving systems as seen in Fig. 7 D. The boundaries between the red group, the yellow group and the green group prevent fluids mixing across the systems. The wells within the boundaries have the feed-zones at the same lithology and depth (except LHD 8 being slightly shallower) (Fig. 15). Thus, we conclude that low permeable boundaries are likely separating the wells and fluid recharge to them. The boundaries might be faults that allow fluid flow along the fault plane but not across. There is also a possibility that the production wells target different zones of the faults or rocks with different mechanical characteristics (more or less fractured). However, the overall fault trends in the area suggest the boundaries are faults. Wells with increasing dryness are located in a system with a lack of recharge. This also can be due to fractured reservoirs which have a low volume porosity. Wells with stable dryness are in a system with adequate recharge. Recharge is even higher near well LHD 11 showing decreasing dryness which indicates a fluid inflow. Hence, the boundaries are between the yellow and the red system (Boundary 1) and the red and the green system (Boundary 2). Surface traces have been observed for Boundary 2 showing a thrust fault and an inferred fault has been mapped coinciding with the location of Boundary 1.

Furthermore, the cross-section of the drying wells correlated with the feed-zones might support the dryness-boundary theory (Fig. 15). It indicates that LHD 8, which is located within the enhanced dryness zones (Fig. 7) has the shallowest feed-zones of all the wells. It could be the reason why LHD 8 dried out faster, leading to around 82 percent of dryness. However, also the wells with deeper feed-zones show a high dryness, such as LHD 15 and LHD 18. Therefore, we think that the depth of feed zones is not the key driver for a rapid dry out. Similarly, LHD 11 and LHD 12, which are in the lower dryness region, have deeper feed zones, resulting in a slower rate of dryness.

The hydrochemistry data as seen in Table 4 suggested a decreasing trend in chloride in LHD 12 and LHD 11. Both wells are in a low-dryness zone and have adequate recharge. They have a lowered chloride level as well as an increase in sulphate. This might be an indicator that the wells receive fluid inflow from the injection site. In contrast, for example in LHD 8, which has dryer conditions, the chloride concentration is rising while the sulphate concentration is dropping.

The pH, electrical conductivity (EC), and mass flow rate indicate similar boundary patterns in the study area (Fig. 16). These parameters further support the earlier indicated boundaries between different dryness zones, especially those between the red and green lines (Fig. 7). Similar tendencies are observed in the mass-flow rate (Fig. 16 C) and pH compartments (Fig. 16 A), showing that LHD 12 acts differently from the drier wells. Furthermore, EC is distinctly different between the wells with the low and the high dryness, meaning that dry wells have roughly twice as much EC . The wells may be separated by the inferred strike-slip fault (Fault A in Fig. 16) and the proven thrust fault near LHD 12 (Fault B in Fig. 16). Two reservoir areas (Fig. 16 A, B) indicate higher values for EC and pH in purple, while the lower values are in blue. Fig. 16 C, suggests a higher mass flow rate in the blue area, whereas the lower mass flow rates are in the purple area. The inferred strike-slip fault striking NE-SW (Fault A) and the confirmed thrust fault striking NW-SE (Fault B) may partition the different fluids in nearby wells, in particular LHD 8, LHD 11, LHD 12, and LHD 18. The faults probably only have a small fracture network associated that prevents the fluids from mixing. This is similarly observed in the dryness pattern as previously explained.

With regards to the field development in Lahendong, the increasing number of the production wells in the southern area compared to the north can be partially due to the presence of more permeable structures. Injection is placed in the north off the main field to prevent reservoir cooling. After long-term utilization some wells in the southern area therefore experience dryness of up to 80% and pressure decline. Possible strategies to address the issue could be: (1) drilling more make up wells in the southern area, (2) placing injection into deep and hot permeable zones far the production wells, or (3) injecting dilute meteoric fluid in the permeable acid wells in the north and try to dilute the acidity and mine heat at the same time.

LHD 8 and LHD 5 receive tracers at around the same time, although LHD 8 is in farther distance than LHD 5 in the north. A permeable structure may be present here, allowing fluids to arrive earlier at farther distances. Near LHD 5, a barrier/low permeability structure may exist, which hinders the tracer to flow, although it has a closer distance. The

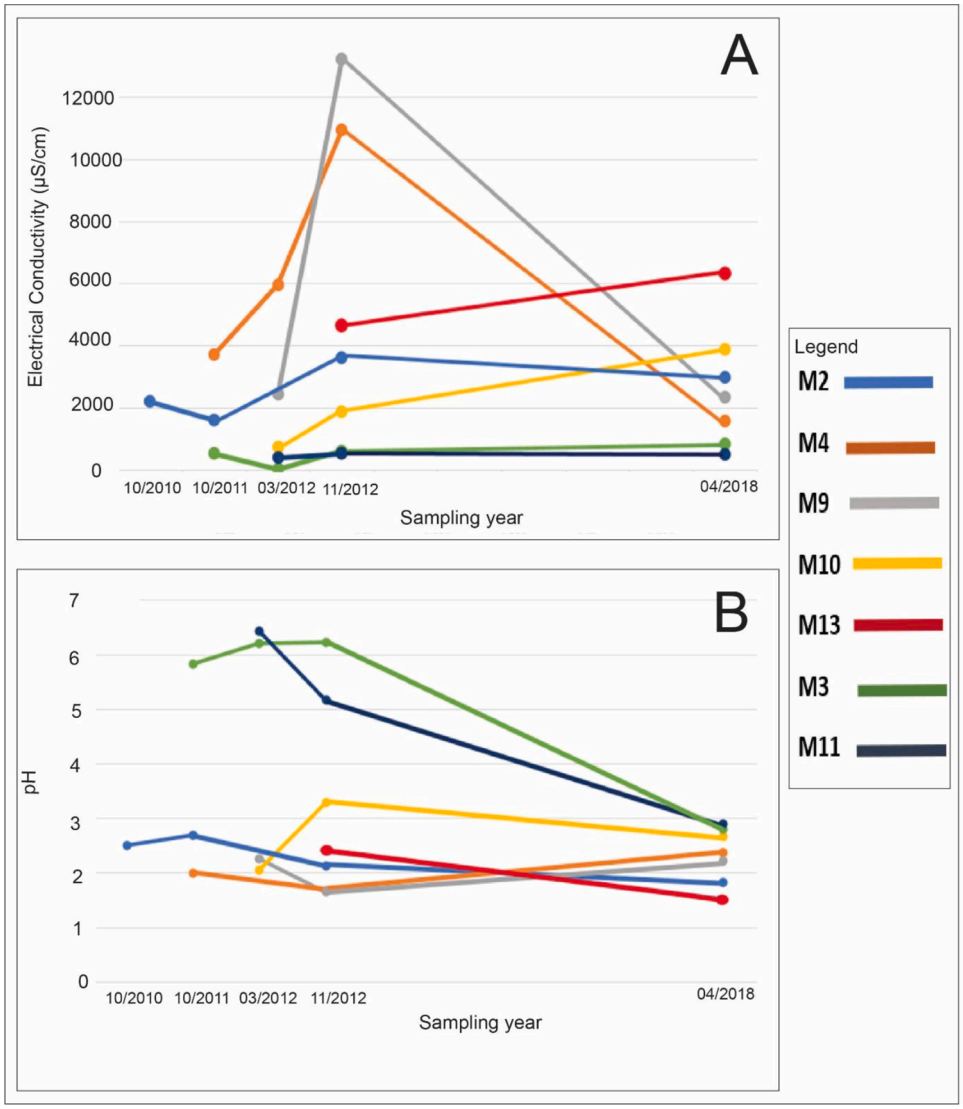


Fig. 14. Temporal changes of Electrical Conductivity (EC) (A) and acidity (pH) for hot springs during 2010-2012, and in 2018 (B)

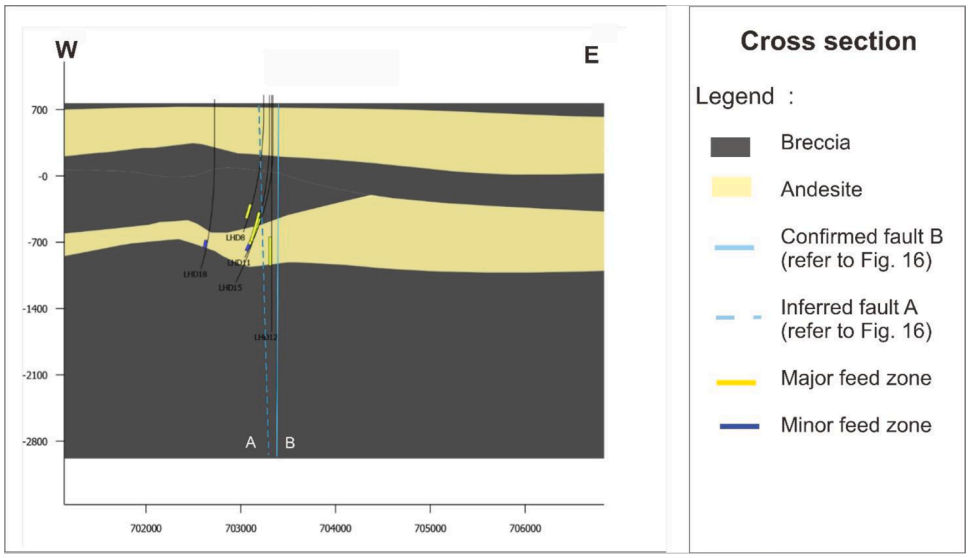


Fig. 15. Cross-section shows shows the wells with increasing dryness in relation to their feed zone depths depths.

Table 4
Chloride concentration for the producing wells with the lower and higher dryness

Well	2012 (mg/l)		2018 (mg/l)	
	Cl	SO_4	Cl	SO_4
LDH 8	347	125	449.08	102.87
LHD 11	337	64	193.04	118.28
LHD 12	466	32	354.52	41.04

slowest tracer breakthrough and maximum peak arrival of tracer in LHD 11 indicates less dispersion, although the well is located at the largest distance from the injector. In general, the different profiles of tracer return between LHD 11 and LHD 8 indicate that the permeability path between LHD 7 and LHD 8 is different, and less direct, than between LHD 7 and LHD 11 as it is sub-parallel with a major fault direction.

The highest mass recovery in LHD 5 occurs probably because the distance from the injector well is only 1.6 km. Hence, it allows a large mass of tracer to reach the well. The second lowest amount of tracer is in LHD 11 with 8×10^{-5} kg/m^3, and the smallest concentration is recovered in LHD 8 with approximately 6×10^{-5} kg/m^3. Interestingly, the mass return in LHD 11 is bigger than LHD 8, consistent with a more direct connection assumed previously, although the distance between injector and LHD 11 is greater than LHD 8. Furthermore, phase return can be another crucial aspect in tracer return patterns. In contrast to the wells producing predominantly steam, the liquid tracer will be detected in wells with low dryness and deeper entry. This suggests the wetter well (LHD 5) has a higher mass flow rate compared to the dryer wells, which have a lower mass flow rate.

Another noteworthy aspect to observe is, in spite of LHD 5 located closest to the injection point (1.6 km), the return times are longer. As a result, injection returns may not be the primary driver of reservoir cooling; rather, more direct flow paths are likely to cool with time. Prabowo et al. (2015) supports this argument with a flow velocity of 4.01E-04 m/s at LHD 5 from calculations based on the tracer profiles. This can be due to less connecting or low permeable fractures being present between the injector and LHD 5 as the producer. The size of fractures is most likely large, allowing for a large injection return to the producer well LHD 5.

Dryness is more prevalent in the southern reservoir for a variety of reasons. The first factor might be the large number of wells drilled in recognized production clusters (clusters 4, 13) in a relatively small area. It could be a major factor why boiling occurs intensively in several producing wells, accompanied by pressure drawdown.

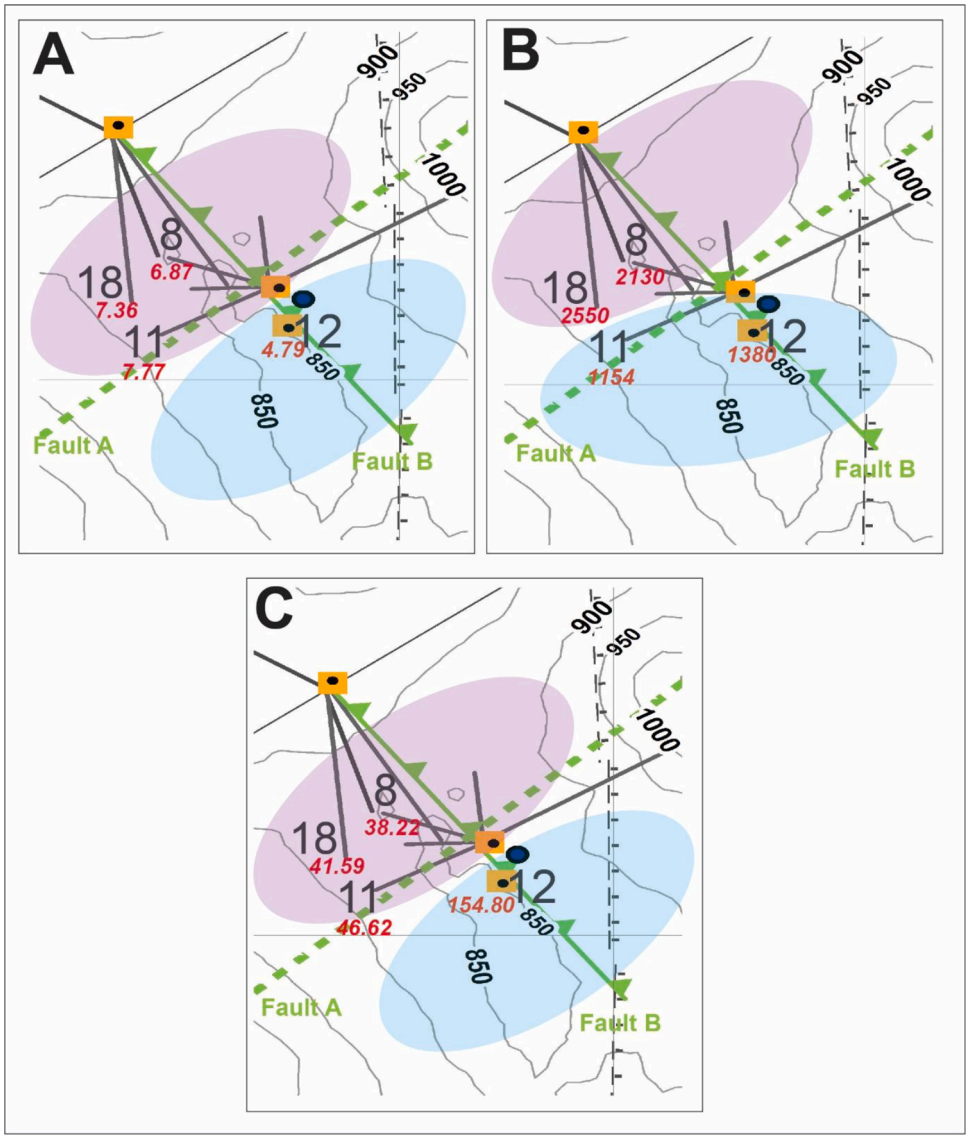


Fig. 16. Patterns of reservoir partitions in the southern wells based on pH (A), EC (B) μS/cm and mass flow rate (tons/hour) (C) (the map symbols as in Fig. 2).

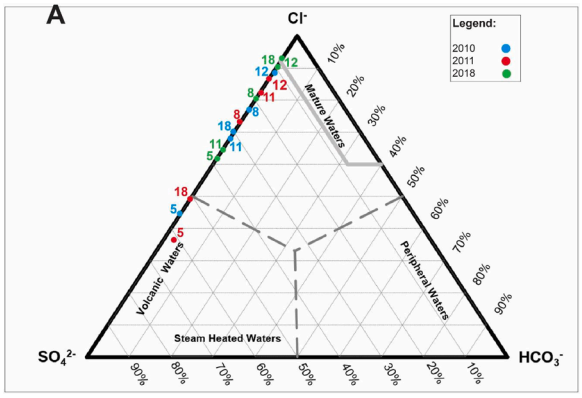


Fig. 17. Ternary plot of relative chloride, sulphate, and bicarbonate concentrations for wells in 2010, 2012 and 2018.

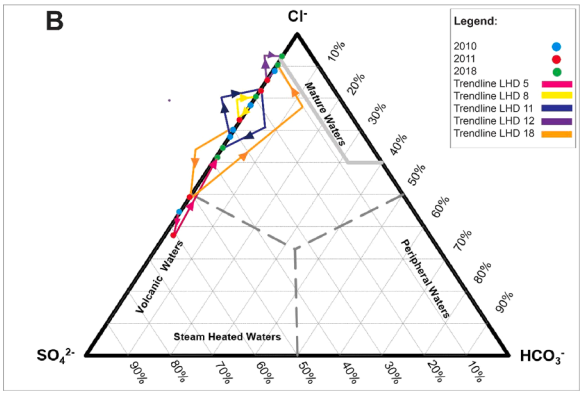


Fig. 18. Ternary plot shows temporal trends for individual wells in 2010, 2011 and 2018.

Overall, the tracer tests reveal a permeability contrast in the subsurface, which could also influence the well dryness and response to the injection. It may be expected that the reservoir (especially in the southern block) may undergo a continuous decline in production capacity and pressure due to pressure drawdown and boiling without proper additional recharge. Moreover, the tracer data analysis shows the presence of a permeability contrast in the subsurface which could cause the well dryness due to missing recharge. These are possible indicators for a continuous decline in production capacity and pressure due to production and boiling without sufficient recharge.

5.2. *Hydrochemistry of Fluids*

In general, a low pH could be due to increasing volcanic degassing of H_2S and /or reservoir boiling. H_2S is an acidic volcanic gas (Lee et al., 2018) and confirmed to be abundant by previous gas analysis in the Lahendong field (Brehme et al., 2016). When the fluid in a geothermal reservoir boils due to pressure drawdown, the H_2S gas travels with the steam. We observe evidence of boiling in an increased steam fraction in the wells. Additionally, the study area is surrounded by active volcanoes in the north and south, a potential source for H_2S (Surachman et al., 1987). An increasing volcanic activity of Mt. Lokon in 2018 may have triggered more H_2S to be released (sources: personal communication; local newspaper (Arief et al., 2018).

The Giggenbach diagram is used to show temporal changes in well waters from 2010, 2011 and 2018 (Figs. 17, 18). The changes suggest waters of acidic sulphate-chloride type during 2010-2011. The origin of the sulphate is by oxidation of H_2S to sulphate, sulphate dissolution from rocks followed by oxidation (Ármannsson, 2009), or degassing and addition of H_2S and SO_2 from volcanoes (Surachman et al., 1987). The change of all wells in 2018 to be more of chloride type indicates increasing concentrations of chloride compared to sulphate and bicarbonate. The increasing chloride in the fluid can be due to boiling. This is also supported by evidence of increasing dryness in some wells (Fig. 7). A good example is LHD 18 with strongly increasing chloride (Fig. 18), continuously increasing EC (Fig. 19 A), increasing dryness (Fig. 7) as well as constantly rising bicarbonate (Fig. 19 C). Moreover, the increase in Cl might also be due to injection returns as provided by the tracer data suggesting the returns directly to LHD 5, LHD 8, and LHD 11. Two latter wells, in particular, had minor changes in dryness, that might also support liquid recharge from injectate.

The temporal evolution of EC, pH and HCO_3 in selected wells (Fig. 19) reflect the dynamics of the reservoir. With respect to electrical conductivity (EC), it appears that most well waters have higher EC. A probable reason behind increasing EC might be boiling as a result of pressure drawdown in the reservoir. The most significant increase in EC occurs in LHD 18 and LHD 5. The strong increase in electrical conductivity of LHD 5 might also be consistent with the tracer returns considering it is the closest well to the injection point, as well as having the largest tracer returns. The slightly decreasing EC values in the few wells (LHD 11, LHD 12) indicate dilution. The boiling as result of major extraction and pressure drawdown in some southern wells (LHD 8, LHD 12, LHD 18) results in increasing dryness. The previous discussion shows that wells LHD 8, LHD 12 and LHD 18 have dryness rates of 40% up to 90% (Fig. 7) in 2013 and 2015. These wells have an increasing EC which correlates with increasing dryness. The increasing pH of well waters over time indicates that the wells are more neutral. The boiling mechanism can induce the raising pH because proton consumption leads to the loss of carbon dioxide (CO_2) (Nicholson, 1993).

A change in fluid pathways in the Lahendong reservoir is observed between the recent study and a previous study (Brehme et al., 2016) as shown in Fig. 20. In contrast to the earlier pattern, which concentrated more in the central region, the latest fluid pathway seems to be more effective in the south-west. The change in the high electrical conductivity pattern is the basis for this interpretation. Also, the lower EC area, which previously extended from the north-east to the south-east, has recently shifted only to the south-eastern region.

6. Conclusion

Production from geothermal fields leads to various changes in the reservoir, e.g. geochemical variations, boiling, changes in dryness or clogging or opening of fluid pathways. In this study, we observed such changes in the long-term operating field in Lahendong in Sulawesi. We used structural-geological mapping, hydrochemical sampling, and well data analysis to integratively understand the reservoir dynamics since start of production.

The recent study validated abundant fault trends: NE-SW trending strike-slip faults, NW-SE trending thrust faults, N-S and E-W trending normal faults. The NE-SW and NW-SE striking are the most dominant faults that control fluid flow in the field. A NW-SE trending thrust fault allows fluids to enter a zone of production near production wells in the southern reservoir. On the other hand, a NE-SW striking fault near LHD 12 appears to be a barrier for fluid flow, observed by dryness behavior, as well as EC, pH and mass flow rate. Less dominant N-S and E-W striking faults seem to allow fluid flow towards production wells in the northern area.

This separation by faults classifies reservoir zones according to their characteristics and behavior. In this study, we found two different compartments in the Lahendong reservoir based on Electrical Conductivity. The boundary between the compartments is a lower permeability zone, which prevents the mixing of fluids. Currently, there are two reservoir zones with higher Electrical Conductivity stretching from the north towards south-west, while the lower Electrical Conductivity is found in the south-east. The current trend changed compared to the

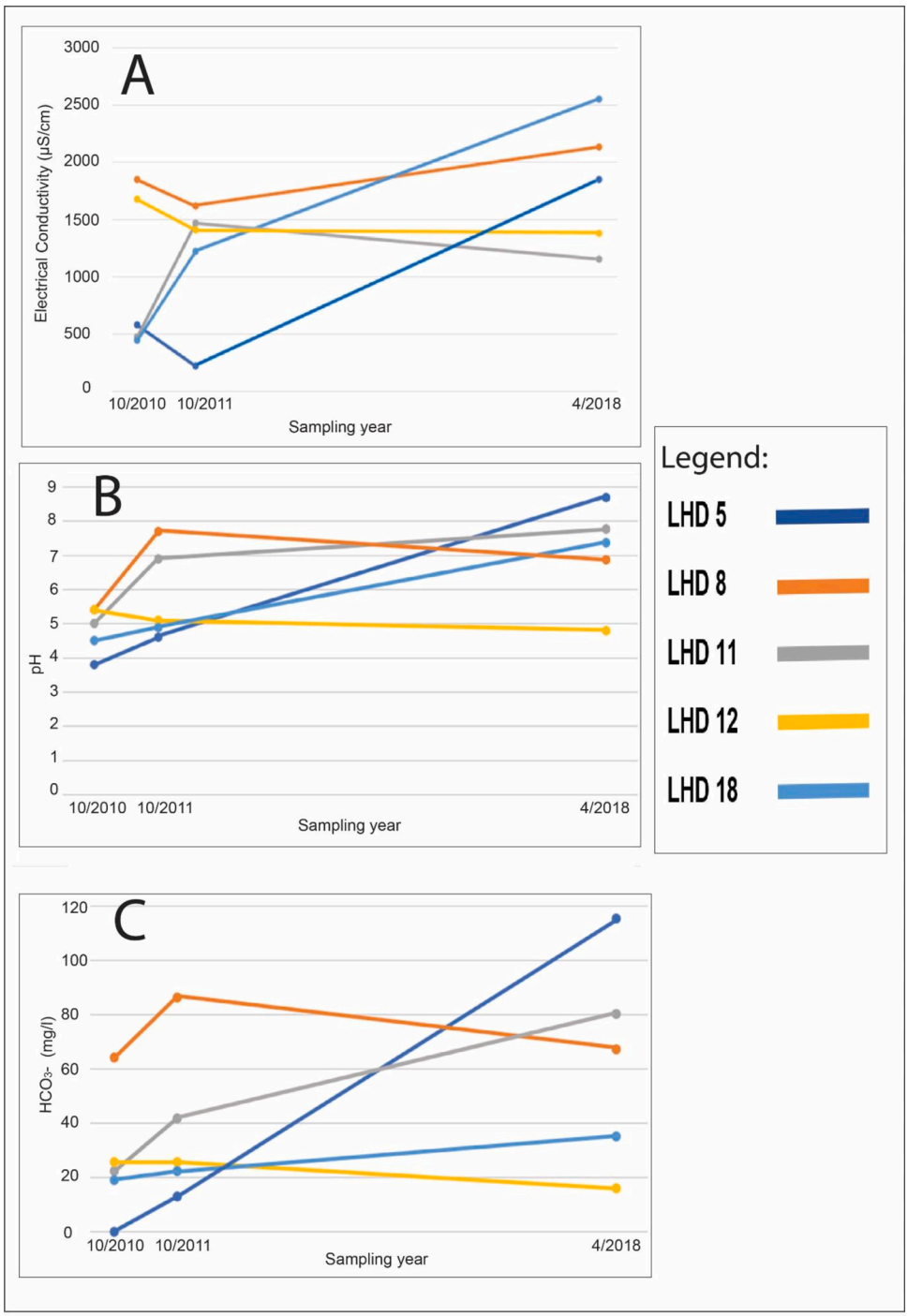


Fig. 19. Temporal changes of electrical conductivity (A), Ph (B) and HCO_3- (C) for well waters.

previous studies as presented by Brehme et al. (2016). That study was showing higher EC fluids concentrated in the central region, whereas the lower EC fluids extended from the north-east to south-east. This phenomenon reflects a change of fluid pathways allowing deep fluids discharge in different areas at the current time.

Lower permeability zones are also observed in the southern reservoir close to production wells LHD 12 and LHD 11. The different dryness behavior of these wells, the pH, electrical conductivity, and mass flow rate show a clear difference across these low permeability zones. Fewer fractures around fault B near to LDH 8 and fault A near to LHD 12 are the reason for the different well behavior.

Also, tracer return profiles unveiled that fracture connectivity in the southern reservoir is more direct than in the north. Wells in the southern zone show, after a similar breakthrough, a sharper signal in the tracer curve than wells in the north. The tracer study shows lower permeability in the north (between LHD 7 and LHD 5), causing a slower tracer flow from injection well LHD 7 to producing well LHD 5.

Boiling as observed in the reservoir is a consequence of the long utilization time. It is observed by time-series of EC showing an increase over time. An increasing concentration of chloride in the wells is also an indicator of boiling. Another study showed the possibility of cooling in some wells based on geothermometers (Suherlina, 2019). As a result of the long-term utilization also surface manifestations have undergone physical and geochemical changes. Temporal analyses show an

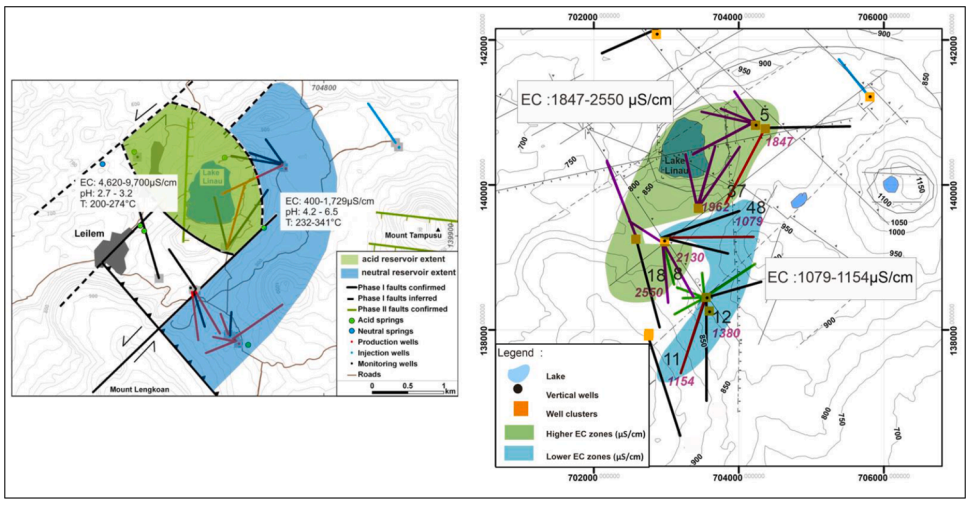


Fig. 20. Fluid pathway changes occured since the former study by Brehme et al., 2016 (left) until the recent study (right) according to changing locations of high and low EC.

increasing acidity and salinity (Suherlina, 2019). The increased gas discharge is possibly due to increasing volcanic activity and/or boiling in the reservoir and closing of fluid pathways letting only gas to discharge. In addition, physical features of hot springs (e.g. ebullition) changed significantly compared to previous years (Suherlina, 2019). This can be induced by tectonic-volcanic, or physical processes (pressure drop, boiling, clogging of permeability). Moreover, the spatial distribution of hot springs presents dynamics of permeability distribution since highly saline waters are concentrated in the central reservoir at the current time compared to previous years when they were expanding into the northwestern region.

Integrating various data sets from this well-observed geothermal field allowed us to conclude on reservoir dynamics caused by long-term operation. Observing and recording reservoir data is highly important to understand the reservoir response to production and ensure the long-term sustainability of the system. The data is critical for a sustainable reservoir management strategy.

CRediT authorship contribution statement

Lily Suherlina: Investigation, Formal analysis, Visualization, Writing – original draft, Writing – review & editing. **Juliet Newson:** Writing – review & editing, Methodology, Conceptualization, Formal analysis. **Yustin Kamah:** Resources, Writing – review & editing. **Maren Brehme:** Conceptualization, Methodology, Software, Supervision, Writing – review & editing, Project administration, Funding acquisition, Validation, Formal analysis.

Declaration of Competing Interest

The authors declare that they have no known competing financial interests or personal relationships that could have appeared to influence the work reported in this paper.

Acknowledgment

The authors acknowledge the team of PT. Pertamina UTC (Upstream Technology Centre), Jakarta and PT. Pertamina Geothermal Energy, Lahendong for support, access to data and to the field. The support of funding on LoLa (Long Term Lahendong Sustainability Use) project from GFZ (German Research Centre for Geoscience) in Potsdam, Germany is deeply appreciated. The authors acknowledge the reviewers for the detailed and helpful comments that improved the manuscript a lot.

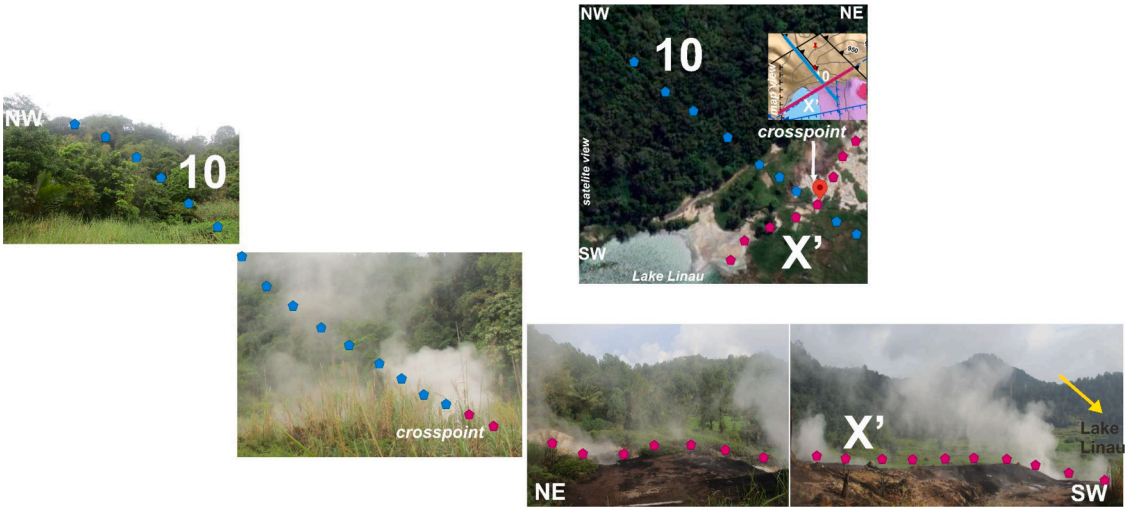
Appendix A

Field evidence shows Crosspoint between surface manifestations as an indicator of intersection point of fault 2 and fault 3.



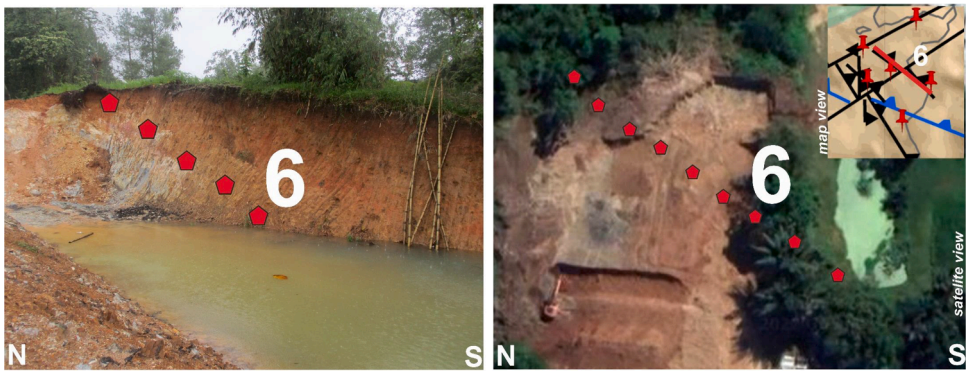
Appendix B

Another example of Crosspoint showing several manifestations present along the intersection point between fault 10 and x'.



Appendix C

Field evidence of fault 6 where fresh unaltered outcrops appear



References

Addison, S.J., Winick, J.A., Sewell, S.M., Buscarlet, E., Hernandez, D., Siega, F.L., 2015. Geochemical Response of the Rotokawa Reservoir to the First 5 Years of Nga Awa Purua Production. In: Proceedings 37th New Zealand Geothermal Workshop. Taupo, pp. 1–11.

Anyim, K., Gan, Q., 2020. Fault zone exploitation in geothermal reservoirs: Production optimization, permeability evolution and induced seismicity. Adv. Geo-Energy Res. 4, 1–12. https://doi.org/10.26804/ager.2020.01.01.

Arief, T., Khafifah, N., Tuwo, A., 2018. Aktivitas Gunung Lokon Meningkat. Kumparan News 1.

Ármannsson, H., 2009. Application of Geochemical Methods in Geothermal Exploration. Lake Naivasha, Kenya.

Arnórsson, S., Stefánsson, A., Bjarnason, J.Ö., 2007. Fluid-fluid interactions in geothermal systems. Rev. Mineral. Geochem. 65, 259–312. https://doi.org/10.2138/rmg.2007.65.9.

Axelsson, G., 2013. Geothermal Well Testing. Reykjavik.

Axelsson, G., 2008. Production Capacity of Geothermal Systems. Tianjin.

Axelsson, G., Björnsson, G., Montalvo, F., 2005. Quantitative Interpretation of Tracer Test Data. In: Proceedings World Geothermal Congress, pp. 24–29.

Axelsson, G., Mortensen, A.K., Franzson, H., 2012. Geothermal Drilling Targets and Well Siting. Santa Tecla, El Salvador.

Brehme, M., 2015. The Role of Fault Zones on Structure, Operation and Prospects of Geothermal Reservoirs-A Case Study in Lahendong, Indonesia. University of Göttingen, Berlin.

Brehme, M., Deon, F., Haase, C., Wiegand, B., Kamah, Y., Sauter, M., Regenspurg, S., 2016. Fault controlled geochemical properties in Lahendong geothermal reservoir Indonesia. Grundwasser 21, 29–41. https://doi.org/10.1007/s00767-015-0313-9.

Brehme, M., Giese, R., Suherlina, L., Kamah, Y., 2019. Geothermal sweetspots identified in a volcanic lake integrating bathymetry and fluid chemistry. Sci. Rep. Nat. Res. 9, 1–10. https://doi.org/10.1038/s41598-019-52638-z.

Brehme, M., Moeck, I., Kamah, Y., Zimmermann, G., Sauter, M., 2014. A hydrotectonic model of a geothermal reservoir - a study in Lahendong, Indonesia. Geothermics 51, 228–239. https://doi.org/10.1016/j.geothermics.2014.01.010.

Burnside, N., Montcoudiol, N., Becker, K., Lewi, E., 2021. Geothermal energy resources in Ethiopia: Status review and insights from hydrochemistry of surface and groundwaters. Wiley Interdiscip. Rev. 8, 1–27. https://doi.org/10.1002/wat2.1554.

Fauzi, A., Permana, H., Indarto, S., Gaffar, E.Z., 2015. Regional structure control on geothermal systems in West Java, Indonesia. In: Proceedings World Geothermal Congress. Melbourne, pp. 1–14.

Gao, Z., Liu, J., Li, F., Wang, M., Feng, J., Wu, G., 2019. Hydrochemical characteristics and temporal variations of geothermal water quality in Tangtou, Shandong, China. Water 11, 1–19. https://doi.org/10.3390/w11081643.

Ghilmana, A., Suryanto, S., Yani, A., 2015. Geothermometer, geoindicator and isotope monitoring in Lahendong Wells during 2010-2012. In: Proceedings World Geothermal Congress. Melbourne, pp. 19–25.

Koestono, H., 2010. Lahendong Geothermal Field, Indonesia: Geothermal Model Based on wells LHD 23 and LHD 28. University of Iceland, Reykjavik.

Koestono, H., Siahaan, E.E., Silaban, M., Franzson, H., 2010. Geothermal model of the lahendong geothermal field, Indonesia. In: Proceedings World Geothermal Congress. Bali, pp. 25–29.

Lecuyer, F., Bellier', O., Gourgaud, A., Vicent, P., 1997. Tectonique active du Nord-Est de Sulawesi (Indorkie) et controle structural de la caldeira de Tondano Active tectonics of north-east Sula wesi (Indonesia) and structural control of the Tondano caldera. Earth Planet. Sci. 325, 607–613.

Lee, S., Kang, N., Park, M., Hwang, J.Y., Yun, S.H., Jeong, H.Y., 2018. A review on volcanic gas compositions related to volcanic activities and non-volcanological effects. Geosci. J. 22, 183–197. https://doi.org/10.1007/s12303-017-0056-y.

Nicholson, K., 1993. Geothermal Fluids Chemistry and Exploration Techniques, 18th ed. Springer-Verlag., Berlin.

Permana, T., Mulyanto, Hartanto, D.B., 2015. Geochemical changes during 12 year exploitation of the southern reservoir zone of Lahendong Geothermal Field, Indonesia. In: Proceedings World Geothermal Congress. Melbourne, pp. 19–25.

Prabowo, T., Yuniar, D.M., Suryanto, S., Silaban, M., 2015. Tracer test implementation and analysis in order to evaluate reinjection effects in Lahendong Field. In: Proceedings World Geothermal Congress. Melbourne, pp. 19–25.

Pratama, H.B., Saptadji, N.M., 2016. Numerical simulation for natural state of two-phase liquid dominated geothermal reservoir with steam cap underlying brine reservoir. In: IOP Conference Series: Earth and Environmental Science. Institute of Physics Publishing. https://doi.org/10.1088/1755-1315/42/1/012006.

Reyes, A.G., Hutt, L., 2000. Petrology and Mineral Alteration in Hydrothermal Systems: From Diagenesis to Volcanic Catastrophes. United Nations University, Geothermal Training Programme, Reykjavik.

Shi, Z., Liao, F., Wang, G., Xu, Q., Mu, W., Sun, X., 2017. Hydrogeochemical characteristics and evolution of hot springs in Eastern Tibetan Plateau Geothermal Belt, Western China: insight from multivariate statistical analysis. Geofluids 2017, 1–12. https://doi.org/10.1155/2017/6546014.

Siahaan, E.E., Soemarinda, S., Fauzi, A., Silitonga, T., Azimudin, T., Raharjo, B., 2005. d, Indonesia. Tectonism and Volcanism Study in the Minahasa Compartment of the North Arm of Sulawesi Related to Lahendong Geothermal Fiel. Proceedings World Geothermal Congress. Ankara, pp. 24–29.

Siratovich, P.A., Heap, M.J., Villeneuve, M.C., Cole, J.W., Kennedy, B.M., Davidson, J., Reuschlé, T., 2016. Mechanical behaviour of the Rotokawa Andesites (New Zealand): Insight into permeability evolution and stress-induced behaviour in an actively utilised geothermal reservoir. Geothermics 64, 163–179. https://doi.org/10.1016/j.geothermics.2016.05.005.

Sugiaman, F., Sunio, E., Molling, P., Stimac, J., 2004. Geochemical response to production of the Tiwi geothermal field, Philippines. Geothermics 33, 57–86. https://doi.org/10.1016/j.geothermics.2003.06.004.

Suherlina, L., 2019. The Dynamic Evolution of Geothermal System in Lahendong, North-Sulawesi, Indonesia (MSc Thesis). Iceland School of Energy, Reykjavik University, Reykjavik.

Sumintadireja, P., Sudarman, S., Zaini, I., 2001. Lahendong geothermal field boundary based on geological and geophysical data. In: Proceedings of the 5th INAGA Annual Scientific Conference and Exhibitions. Yogyakarta, pp. 1–8.

Surachman, S., Tandirerung, S.A., Buntaran, T., Robert, D., 1987. Assessment of the Lahendong geothermal field, North Sulawesi, Indonesia. In: Proceedings World Geothermal Congress, pp. 19–25.

Truesdell, A.H., Stallard, M.L., Trujillo, P.E., Counce, D., Janik, C.J., Winnett, T.L., Goff, F., Shenevell, L., 1987. Interpretation of fluid chemistry from the PLTG-1 exploratory drill hole, Platanares. Honduras. In: PROCEEDINGS, 12th Workshop on Geothermal Reservoir Engineering. Standford, pp. 1–6.

Utami, P., Browne, P.R.L., Simmons, S.F., Suroto, A., 2007. Lahendong and some other geothermal systems in the Western Pacific Belt: comparison on their geologic settings, hydrology and hydrothermal alteration. In: Proceedings 29th NZ Geothermal Workshop . NZ Geothermal Workshop, Auckland, pp. 1–9.

Utami, P., Siahaan, E., Azimudin, T., Browne, P., Simmons, S., 2004. Overview of the Lahendong Geothermal Field, North Sulawesi, Indonesia : a progress report. In: Proceedings 26th NZ Geothermal Workshop 2004, pp. 1–6.

Wang, C., Zheng, M., 2019. Hydrochemical characteristics and evolution of hot fluids in the gudui geothermal Field in Comei County, Himalayas. Geothermics 81, 243–258. https://doi.org/10.1016/j.geothermics.2019.05.010.

Yani, A., 2006. Numerical Modelling of Lahendong Geothermal System, Indonesia. Reykjavik.